*nanomaterials*

MDPI

*Article*

# The Combined Effects of an External Field and Novel Functional Groups on the Structural and Electronic Properties of TMDs/$Ti_3C_2$ Heterostructures: A First-Principles Study

**Siyu Zheng [1], Chenliang Li [1,*], Chaoying Wang [1], Decai Ma [2] and Baolai Wang [1]**

[1] College of Aerospace and Civil Engineering, Harbin Engineering University, Harbin 150001, China
[2] School of Physics and Engineering, Sun Yat-sen University, Guangzhou 510275, China
* Correspondence: lichenliang@hrbeu.edu.cn

**Abstract:** The stacking of $Ti_3C_2$ with transition metal dihalide (TMDs) materials is an effective strategy to improve the physical properties of a single material, and the tuning of the related properties of these TMDs/$Ti_3C_2$ heterostructures is also an important scientific problem. In this work, we systematically investigated the effects of an external field and novel functional groups (S, Se, Cl, Br) on the structural and electronic properties of TMDs/$Ti_3C_2X_2$ heterostructures. The results revealed that the lattice parameters and interlayer distance of TMDs/$Ti_3C_2$ increased with the addition of functional groups. Both tensile and compressive strain obviously increased the interlayer distance of $MoS_2/Ti_3C_2X_2$ (X = S, Se, Cl, Br) and $MoSe_2/Ti_3C_2X_2$ (X = Se, Br). In contrast, the interlayer distance of $MoSe_2/Ti_3C_2X_2$ (X = S, Cl) decreased with increasing compressive strain. Furthermore, the conductivity of TMDs/$Ti_3C_2$ increased due to the addition of functional groups (Cl, Br). Strain caused the bandgap of TMDs to narrow, and effectively adjusted the electronic properties of TMDs/$Ti_3C_2X_2$. At 9% compressive strain, the conductivity of $MoSe_2/Ti_3C_2Cl_2$ increased significantly. Meanwhile, for TMDs/$Ti_3C_2X_2$, the conduction band edge (CBE) and valence band edge (VBE) at the M and K points changed linearly under an electric field. This study provides valuable insight into the combined effects of an external field and novel functional groups on the related properties of TMDs/$Ti_3C_2X_2$.

**Keywords:** TMDs/MXenes; electronic properties; density functional theory (DFT); functional groups; biaxial strain; electric field

check for updates

**Citation:** Zheng, S.; Li, C.; Wang, C.; Ma, D.; Wang, B. The Combined Effects of an External Field and Novel Functional Groups on the Structural and Electronic Properties of TMDs/$Ti_3C_2$ Heterostructures: A First-Principles Study. *Nanomaterials* **2023**, *13*, 1218. https://doi.org/10.3390/nano13071218

Academic Editor: Lyubov G. Bulusheva

Received: 16 February 2023
Revised: 22 March 2023
Accepted: 28 March 2023
Published: 29 March 2023



## 1. Introduction

Due to the inter-layer coupling effect, heterostructures formed by vertically stacking different two-dimensional (2D) materials can achieve ultra-high-performance improvements and possess unprecedentedly excellent physical properties [1–3]. The transition metal dihalides (TMDs) have excellent band gap widths in the range of 1.0 eV to 2.0 eV [4]. The monolayer $MoS_2$, as a typical representative member of the most studied TMD family, is a semiconductor material with a direct band gap of 1.8 eV, and it is widely used in logic transistors and photodetector devices [5,6]. Similarly, the monolayer $MoSe_2$, as another important member of TMDs, has many promising applications in electronics and optoelectronics due to its unique electronic, optical, mechanical, chemical, and thermal properties [7,8]. However, TMDs also have some negative properties that affect their application. For example, their carrier effective mass is relatively high, while the carrier mobility is very low [9,10], which hinders their application in high-performance nanodevices. Several studies have shown that the heterogeneous structures formed by stacking TMDs with other 2D materials can significantly modulate the structural, electronic, and mechanical properties of TMDs. For example, the studies of Biroju et al. [11] showed that $MoS_2$ stacked with a bilayer graphene heterostructure can improve electronic conductivity, electrochemical properties, and photochemical properties. Li et al. [12] systematically investigated electron density differences and band gaps of $Cu_3N/MoS_2$ heterostructures, and

the results showed that the charge was mainly accumulated and consumed near the atoms, with only a small amount of charge accumulating between the layers, and the bandgap of $Cu_3N/MoS_2$ heterostructures can be efficiently tuned with the variation of the interlayer distance. Moreover, $Cu_3N/MoS_2$ heterostructures have a stable structure and excellent photoelectric properties. Celal et al. [13] investigated the structural and electronic properties of $GaN/MoSe_2$ heterostructures with van der Waals (vdW) correction. An indirect band gap of 1.371 eV was obtained when the GaN monolayers were adsorbed on $MoSe_2$ monolayers, while when GaN was stacked on $MoSe_2$ monolayers, the indirect band gap in GaN monolayers was maintained at 0.341 eV. Based on these studies, we can conclude that combining TMDs with other two-dimensional layered materials to form heterogeneous structures may be an effective way to tune and improve the relevant properties of TMDs.

MXenes are a new and important member of the family of 2D materials discovered in recent years and are complex layered 2D material systems representing a large class of transition metal nitriles, carbides, and carbonitrides [14–16]. $Ti_3C_2$ is a typical transition metal carbide with multilayer metal ion adsorption behavior, with ultra-high electrical conductivity and extraordinary mechanical and electronic properties [17,18]. $Ti_3C_2$ is expected to be the most competitive material candidate in some fields, such as high-performance ultra-thin electronics and storage [19,20]. Mathis et al. [21] investigated the MXene nanosheets (Al-$Ti_3C_2$), and found they have higher quality, increased oxidation resistance, and electronic conductivity increased to 20,000 S/cm. Al-$Ti_3C_2$ is a promising electric nanodevice. Li et al. [22] systematically investigated the interfacial properties of monolayer $WS_2$ in contact with a series of MXenes using first-principles calculations. The results showed that $Ti_3C_2$ couples strongly with $WS_2$, leading to the metallization of monolayer $WS_2$ and the formation of ideal Ohmic contacts in the vertical direction. Moreover, during the electrode fabrication process, the face-to-face stacking of 1 nm thickness MXene limits the accessibility to electrolyte ions [23,24], which hinders the electronic properties utilization of its surface. For $Ti_3C_2$, heterostructure stacking is also a valuable tool for improving the electronic properties since it can not only add the excellent properties of a single 2D material but also provide a stable gallery space [25–27], which could prevent face-to-face stacking of MXene. For example, Wu et al. [28] systematically investigated the energy storage and electronic properties of N-$Ti_3C_2/NiCo_2S_4$ heterostructures. Owing to the unique heterostructure and friendly interfacial interaction, the N-$Ti_3C_2/NiCo_2S_4$ heterostructure had a stable structure, low internal resistance, and excellent rate performance. Debow et al. [29] found that the strong electronic coupling between $Ti_3C_2O_x$ and $TiO_2$ is due to their proximity; the $Ti_3C_2O_x$-generated electrons are transferred into the conduction band of the $TiO_2$ semiconductor over the Schottky barrier with a fast time constant of 180 fs, leading to an increase in conductivity.

Currently, there are a large number of studies on TMD and MXene heterostructures. Jing et al. [30] systematically investigated the structural and electronic properties of $MoS_2/Ti_3C_2T_x$ (T = OH, F and O) heterostructures, and the results showed that the $MoS_2/Ti_3C_2F_2$ heterostructure is an *n*-type Schottky contact and the Schottky barrier height (SBH) is 0.73 eV, while the $MoS_2/Ti_3C_2O_2$ heterostructure is a *p*-type Schottky contact with an SBH of 0.33 eV. Moreover, the tensile strain can effectively adjust the position of the conduction band edge (CBE) of $MoS_2$, which leads to an effective reduction of the Fermi energy level pinning and SBH, thus allowing for Ohmic contact. Guan et al. [31] studied heterostructures composed of $Ti_3C_2T_2$ (T = O and F atoms) and metallic $MoS_2$ (1T phase) for lithium-ion battery (LIB) applications. The different surface functional groups in MXenes were found to significantly alter the redox reaction of Li atoms in the $Ti_3C_2T_2$ and 1T-$MoS_2$ interfaces. The diffusion curve became significantly flattened from the bared to O and F terminated $Ti_3C_2$, with the Schottky barrier height reducing dramatically from 0.80 eV to 0.22 eV and 0.29 eV, respectively. The surface functional group O or F can remove the spatial site resistance of Li embedding by disrupting the strong interaction between the two layers while providing additional adsorption sites for Li diffusion. Li et al. [32] found that $MoS_2/Ti_2C$ heterostructures have good thermoelectric and transport properties, and the

applied electric field or strain can significantly improve their thermoelectric and transport properties. Xu et al. [33] found that $MoSe_2/Ti_3C_2T_x$ (T = OH, O, and F) heterostructures exhibit excellent electrochemical properties at very high currents and have a large potential for sodium ion storage, which can be applied to high-performance sodium–ion batteries. Ling et al. [34] demonstrated by a first-principles method that $MoS_2/Ti_3C_2$–OH heterostructures can enhance the catalytic activity of $MoS_2$ at low sulfur vacancy concentrations. Combining the $MoS_2/Ti_3C_2$-OH heterostructure with strain engineering can realize the potential of efficient hydrogen production. Based on these previous studies, TMDs/MXenes heterostructures can improve the related properties of single TMDs or MXenes, and the surface functional groups of the monolayer MXenes are an effective way to tune the properties of the TMDs/MXenes heterostructures. However, these studies have mainly focused on the surface functional groups O, F, and OH.

Recently, Kamysbayev et al. [35] successfully synthesized MXenes with novel functional groups (S, Se, Cl, Br, Te) capped with $Ti_3C_2$, all of which showed in-plane tensile strain, especially $Ti_3C_2Te_2$, which had the maximum in-plane tension, showing in-plane lattice expansion of more than 18%. Lattice expansion promoted the appearance of $Ti_3C_2$ electron mobility over $10^4$ $cm^2/V{\cdot}s$ at room temperature, as well as superconductivity. Based on the studies of Kamysbayev et al. [35], it can be concluded that these novel functional groups (S, Se, Cl, Br) obviously induce a change in the related properties of $Ti_3C_2$. Moreover, as we know, the external field can induce fancy changes in the properties of 2D materials. However, it is still unclear about the effects of these novel functional groups (S, Se, Cl, Br) and external fields on the structural and electronic properties of the TMDs/$Ti_3C_2$ heterostructures. In this paper, we first systematically investigated the structural and electronic properties of these TMDs/$Ti_3C_2X_2$ (X = S, Se, Cl, Br) heterostructures using the density functional theory (DFT), and discussed in detail the effects of these novel surface functional groups on the related properties of these TMDs/$Ti_3C_2$ heterostructures. In addition, we then further explored the effect of external biaxial strain and electric field on the structural and electronic properties of these TMDs/$Ti_3C_2X_2$ heterostructures.

## 2. Calculation Method

All calculations were performed within the framework of density functional theory using the CASTEP code [36]. The Perdew–Burke–Ernzerhof (PBE), based on the generalized gradient approximation (GGA), was used as the exchange–correlation function [37]. In order to accurately represent the van der Waals interactions between monolayer TMDs and 2D $Ti_3C_2$, a semi-empirical dispersion correction in Grimme format (DFT–D) was used [38]. The Ultrasoft pseudopotential [39] was used to describe the ion–electron interaction. The valence electrons performed as the [Ar]3p3d4s configuration for the Ti atom, the [Ne]3s3p configuration for the S and Cl atoms, the [Kr]4d5s configuration for the Mo atom, the [He]2s2p configuration for the C atom, and the [Ar]4p4s configuration for Br and Se atoms. The energy cutoff was set to 450 eV [40]. Structural optimization was performed using a $9 \times 9 \times 1$ Monkhorst–Pack grid *K*-point sampling in the Brillouin zone in the unit cell, with the optimization energy convergence parameter set to $10^{-5}$ eV/atom and the force convergence parameter on the atoms set to 0.03 eV/Å [41]. The *K*-point grid was increased to $11 \times 11 \times 1$ for the calculation of energy bands and density of states [42]. A vertical vacuum layer thickness of more than 15 Å was set to prevent periodic boundary interactions between adjacent layers [43]. The binding energy of the TMDs/$Ti_3C_2$ heterostructure was defined as:

$$E_b = \left(E_{TMDs/Ti_3C_2} - E_{Ti_3C_2} - E_{TMDs}\right)/A$$

where $E_{TMDs/Ti_3C_2}$, $E_{Ti_3C_2}$, and $E_{TMDs}$ are the total energies of the heterostructure, bare $Ti_3C_2$, and the TMD monolayer, respectively, and $A$ is the interface area [44]. We not only investigated the structural and electronic properties of pristine TMDs/$Ti_3C_2$ and TMDs/$Ti_3C_2X_2$ (X = S, Se, Cl, Br) but also explored the effect of biaxial strain on the

structural and electronic properties of TMDs/$Ti_3C_2$ and TMDs/$Ti_3C_2X_2$ (X = S, Se, Cl, Br) heterostructures. The biaxial strain was defined as:

$$\varepsilon_x = (a - a_0)/a_0 \times 100\%$$

$$\varepsilon_y = (b - b_0)/b_0 \times 100\%$$

where and $a_0$ are the $x$-axis lattice constants in the presence and absence of strain, respectively; and $b$ and $b_0$ are the $y$-axis lattice constants in the presence and absence of strain, respectively [45]. In addition, positive (negative) values indicate tensile (compressive) strain. All heterostructure structures were relaxed.

## 3. Results and Discussions

### *3.1. Structural Properties of the TMDs/$Ti_3C_2$ Heterostructures*

The lattice constants of our optimized $MoS_2$, $MoSe_2$, and $Ti_3C_2$ monolayers were 3.15 Å, 3.24 Å and 3.12 Å, respectively, which were in good agreement with the previous studies [46,47]. They all have a hexagonal crystal structure with a space group of P63/mmc, and they possess a lattice mismatch rate within a reasonable range of less than 4%, allowing the construction of heterostructures [48]. According to the high-symmetry stacking mode, there are six possible TMDs/$Ti_3C_2$ configurations, taking $MoS_2$/$Ti_3C_2$ heterostructures as an example, see Figure 1 (six high-symmetry $MoSe_2$/$Ti_3C_2$ heterostructures, see Figure S1): (a) the ZM_SA Configuration: S and Mo atoms of $MoS_2$ are on top of Ti and C atoms of $Ti_3C_2$, respectively; (b) the ZM_AA Configuration: S and Mo atoms of $MoS_2$ are on top of C and Ti atoms of $Ti_3C_2$, respectively; (c) the ZM_AS Configuration: S and Mo atoms of $MoS_2$ are on top of Ti atoms and hollow sites of $Ti_3C_2$, respectively; (d) the MZ_SA Configuration: S and Mo atoms of $MoS_2$ are on top of C atoms and hollow sites of $Ti_3C_2$, respectively; (e) the MZ_AA Configuration: Mo and S atoms of $MoS_2$ are on top of C atoms and hollow sites of $Ti_3C_2$, respectively; (f) the MZ_AS Configuration: Mo and S atoms of $MoS_2$ are on top of Ti atoms and hollow sites of $Ti_3C_2$, respectively.

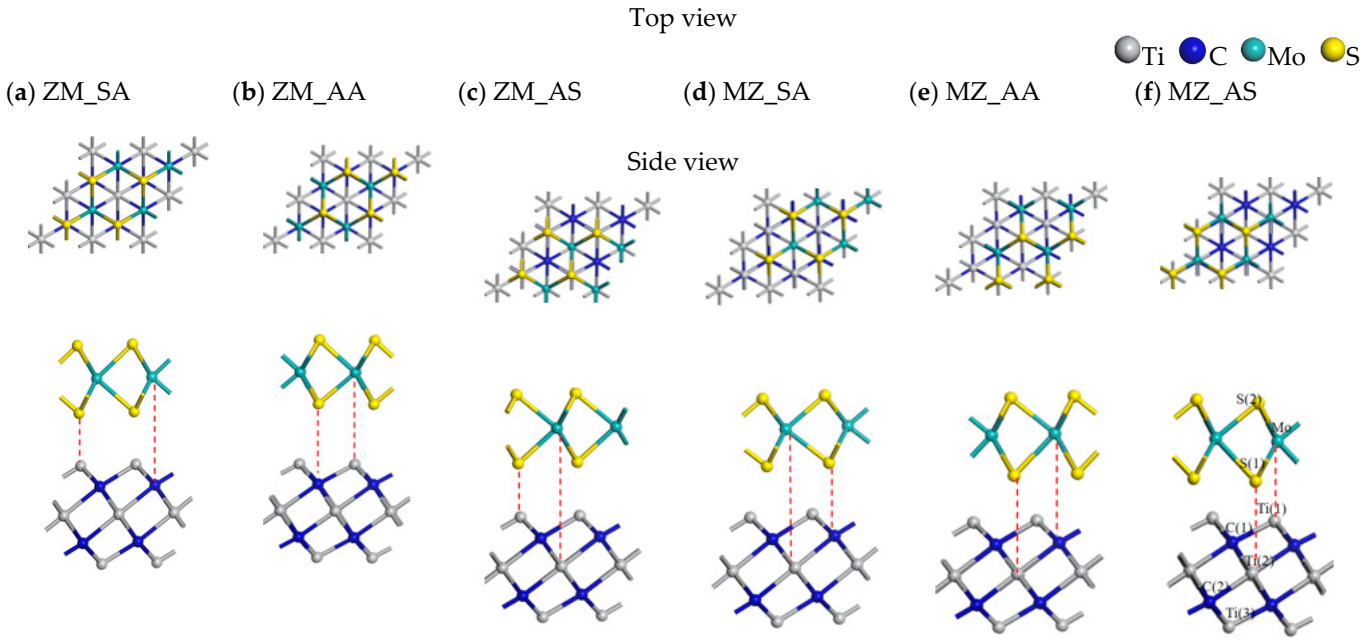


**Figure 1.** A schematic diagram of top and side views of $MoS_2$/$Ti_3C_2$ heterostructures for different stackings. (**a**) the ZM_SA Configuration; (**b**) the ZM_AA Configuration; (**c**) the ZM_AS Configuration; (**d**) the MZ_SA Configuration; (**e**) the MZ_AA Configuration; (**f**) the MZ_AS Configuration.

Table 1 lists our calculated binding energies, interlayer distance, and bond lengths for the six possible stacking configurations of $MoS_2/Ti_3C_2$ heterostructures. It can be seen that the binding energies of these $MoS_2/Ti_3C_2$ heterostructures were all negative, indicating that the formation of all the heterostructures was exothermic. A lower binding energy represents a more stable heterostructure structure. The ZM_SA configuration of $MoS_2/Ti_3C_2$ had the lowest binding energy of −1.79 meV/Å, so it was energetically the most stable configuration among the six configurations. It is noted that the interlayer distance *d* of the $MoS_2/Ti_3C_2$ heterostructure was very small (in the range of 1.68 Å to 2.47 Å), which indirectly indicated a strong interaction between the layers [49,50]. Table 2 presents the binding energy of −1.03 meV/Å for the most stable configuration SA_ZM of the $MoSe_2/Ti_3C_2$ heterostructure, while the AS_ZM configuration had the maximum binding energy of −0.39 meV/Å. The binding energies of all six configurations were negative, indicating the stability of the $MoSe_2/Ti_3C_2$ heterostructure. The interlayer distance *d* of the six configurations of $MoSe_2/Ti_3C_2$ heterostructures ranged from 1.89 Å to 2.56 Å, which was similar to that of $MoS_2/Ti_3C_2$ heterostructures.

**Table 1.** Binding energy ($E_b$), interlayer distance (*d*), Mo–S(1) minus Mo–S(2) constant ($d_{12}$), and bond lengths Ti–C ($d_{Ti–C}$) for $MoS_2/Ti_3C_2$ heterostructures, respectively.

| Configurations | $E_b$ (meV/Å$^2$) | *d* (Å) | $d_{12}$ (Å) | $d_{Ti(3)–C(2)}$ (Å) | $d_{Ti(1)–C(1)}$ (Å) |
|---|---|---|---|---|---|
| (a) ZM_SA | −1.79 | 1.68 | 0.069 | 2.059 | 2.125 |
| (b) ZM_AA | −1.21 | 1.69 | 0.078 | 2.057 | 2.152 |
| (c) ZM_AS | −1.42 | 2.47 | 0.031 | 2.058 | 2.069 |
| (d) MZ_SA | −1.27 | 2.03 | 0.109 | 2.055 | 2.094 |
| (e) MZ_AA | −1.48 | 1.92 | 0.134 | 2.057 | 2.081 |
| (f) MZ_AS | −1.55 | 2.46 | 0.021 | 2.063 | 2.067 |

**Table 2.** Binding energy ($E_b$), interlayer distance (*d*), Mo–Se(1) minus Mo–Se(2) constant ($d_{34}$), and bond lengths Ti–C ($d_{Ti–C}$) for $MoSe_2/Ti_3C_2$ heterostructures, respectively.

| Configurations | $E_b$ (meVÅ$^2$) | *d* (Å) | $d_{34}$ (Å) | $d_{Ti(3)–C(2)}$ (Å) | $d_{Ti(1)–C(1)}$ (Å) |
|---|---|---|---|---|---|
| (g) SA_ZM | −1.03 | 1.89 | 0.051 | 2.064 | 2.119 |
| (h) AA_ZM | −1.01 | 2.56 | 0.013 | 2.071 | 2.073 |
| (i) AS_ZM | −0.39 | 2.51 | 0.021 | 2.067 | 2.074 |
| (j) SA_MZ | −0.76 | 2.12 | 0.101 | 2.061 | 2.096 |
| (k) AA_MZ | −0.96 | 2.09 | 0.107 | 2.068 | 2.083 |
| (m) AS_MZ | −0.59 | 2.01 | 0.063 | 2.069 | 2.122 |

A comparison of the data in Tables 1 and 2 showed that the binding energies of all these $MoS_2/Ti_3C_2$ heterostructures were smaller than those of the corresponding $MoSe_2/Ti_3C_2$ heterostructures; meanwhile, $MoS_2/Ti_3C_2$ had a smaller interlayer distance than the $MoSe_2/Ti_3C_2$ heterostructures. These findings showed that the $MoS_2/Ti_3C_2$ heterostructures are more stable. We calculated the Ti–C bond length in the original monolayer $Ti_3C_2$ as 2.057 Å. As shown in Tables 1 and 2, the Ti(3)–C(2) bond length $d_{Ti(3)–C(2)}$ showed almost no change, but the Ti(1)–C(1) bond lengths of the upper layer of $Ti_3C_2$ were stretched in the TMDs/$Ti_3C_2$ heterostructures. The reason for this may be that the charge transfer from $Ti_3C_2$ to TMDs leads to the stretching of the Ti(1)–C(1) bond. The Mo–S(1) minus Mo–S(2) value ($d_{12}$) and Mo–Se(1) minus Mo–Se(2) value ($d_{34}$) are also presented in Tables 1 and 2. $d_{12}$ ranged from 0.021 Å to 0.134 Å, and $d_{34}$ ranged from 0.013 Å to 0.107 Å, indicating that the TMDs/$Ti_3C_2$ heterostructure slightly destabilizes the TMDs monolayer. Moreover, the $d_{12}$ values in the $MoS_2/Ti_3C_2$ heterostructure were all greater than the $d_{34}$ in the $MoSe_2/Ti_3C_2$ heterostructure, suggesting that the interlayer electron coupling effect of $MoS_2/Ti_3C_2$ is greater than that of $MoSe_2/Ti_3C_2$. This conclusion was consistent with the results of our calculated interlayer distance and binding energy. We also noted that the binding energy and interlayer distance of the ZM_SA configurations were the smallest, so

the ZM_SA configuration is the most stable configuration among the 12 configurations of $MoS_2/Ti_3C_2$ heterostructures and $MoSe_2/Ti_3C_2$ heterostructures considered here.

We also further investigated the effects of novel functional groups (S, Se, Cl, Br) on the structural properties of TMDs/$Ti_3C_2$ heterostructures. Previous experimental studies [51] have shown that the $Ti_3C_2X_2$ (X = S, Se, Cl, Br) are the most stable when the surface functional groups of $Ti_3C_2$ are located in the cavity centers of Ti atoms and aligned perpendicularly to the Ti atoms in the middle layer because of the site-blocked repulsion reaction between the C atoms and the surface functional groups. Therefore, in this work, when the surface of $Ti_3C_2$ was terminated by functional groups (S, Se, Cl, Br) in $MoS_2/Ti_3C_2X_2$ and $MoSe_2/Ti_3C_2X_2$ heterostructures, we focused on the case that the functional groups are located above the hole center of the Ti atom and perpendicular to the middle Ti atom, as shown in Figure 2a,b, respectively.

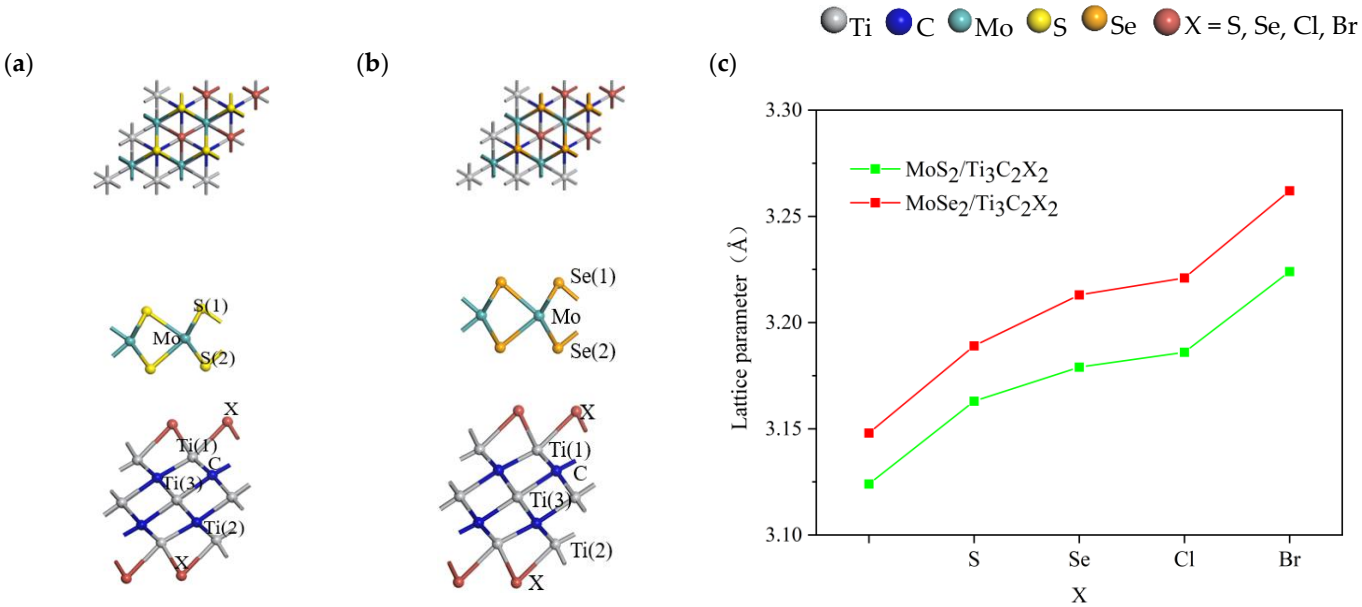


**Figure 2.** Structural properties of TMDs/$Ti_3C_2X_2$ heterostructures. (**a**) Diagram of top and side views of $MoSe_2/Ti_3C_2X_2$ heterostructures; (**b**) Diagram of top and side views of $MoS_2/Ti_3C_2X_2$ heterostructures; (**c**) The lattice parameters of TMDs/$Ti_3C_2X_2$ heterostructures.

It can be clearly observed from Figure 2c that the lattice parameters of TMDs/$Ti_3C_2X_2$ heterostructures changed significantly due to the addition of surface functional groups. The lattice parameter of the $MoS_2/Ti_3C_2$ heterostructure was 3.124 Å. With the addition of each functional group, the lattice parameter obviously increased, and $MoS_2/Ti_3C_2Br_2$ had the maximum lattice parameter of 3.224 Å. The lattice parameter of $MoS_2/Ti_3C_2S_2$, $MoS_2/Ti_3C_2Se_2$ and $MoS_2/Ti_3C_2Cl_2$ increased to 3.163 Å, 3.179 Å and 3.186 Å, respectively. Similarly, the lattice parameters of the $MoSe_2/Ti_3C_2$ heterostructure increased with the addition of functional groups. The lattice parameters of the $MoSe_2/Ti_3C_2$ heterostructure were 3.148 Å, while $MoSe_2/Ti_3C_2S_2$, $MoSe_2/Ti_3C_2Se_2$, $MoSe_2/Ti_3C_2Cl_2$, and $MoSe_2/Ti_3C_2Br_2$ were 3.189 Å, 3.213 Å, 3.221 Å, and 3.262 Å, respectively. Therefore, the surface functional groups had a significant effect on the structural properties of $MoS_2/Ti_3C_2X_2$ and $MoSe_2/Ti_3C_2X_2$.

To further understand the stability of these TMDs/$Ti_3C_2X_2$ heterostructures, we calculated the binding energy, interlayer distance, and structural parameters of TMDs/$Ti_3C_2X_2$ (X = S, Se, Cl, Br) as shown in Table 3. We provide the coordinates of the TMDs/$Ti_3C_2X_2$ (X = S, Se, Cl, Br) optimized structure in the Supplementary Materials, see Table S1. The binding energies of $MoS_2/Ti_3C_2X_2$ and $MoSe_2/Ti_3C_2X_2$ were negative. The $MoSe_2/Ti_3C_2Cl_2$ heterostructure possessed the highest binding energy (−3.12 meV/Å), while the $MoS_2/Ti_3C_2S_2$ heterostructure had the lowest binding energy (−8.44 meV/Å), indicating that the $MoS_2$/

$Ti_3C_2S_2$ heterostructure was more stable. The interlayer distance of these heterostructures varied from 2.78 Å to 3.14 Å, which was significantly larger than that of the TMDs/$Ti_3C_2$ heterostructure, and a larger interlayer distance indicated a weaker electronic coupling between the monolayer TMDs and $T_3C_2X_2$. It can be concluded that $MoS_2/Ti_3C_2X_2$ and $MoSe_2/Ti_3C_2X_2$ are typical van der Waals heterostructures.

**Table 3.** Binding energy ($E_b$), interlayer distance ($d$), Mo–S(1) minus Mo–S(2) or Mo–Se(1) minus Mo–Se(2) constant ($d_{56}$), and bond lengths Ti–X $d_{Ti–X}$ and Ti–C $d_{Ti–C}$ for TMDs/$Ti_3C_2X_2$ (X = S, Se, Br, Cl) heterostructures, respectively.

| Configurations | $E_b$ (meVÅ$^2$) | $d$ (Å) | $d_{56}$ (Å) | $d_{Ti(1)–C}$ (Å) | $d_{Ti(2)–X}$ (Å) | $d_{Ti(1)–X}$ (Å) |
|---|---|---|---|---|---|---|
| $MoS_2/Ti_3C_2S_2$ | −8.44 | 2.83 | 0.009 | 2.182 | 2.397 | 2.389 |
| $MoS_2/Ti_3C_2Se_2$ | −3.95 | 2.78 | 0.007 | 2.146 | 2.520 | 2.496 |
| $MoS_2/Ti_3C_2Cl_2$ | −3.17 | 3.02 | 0.003 | 2.104 | 2.503 | 2.492 |
| $MoS_2/Ti_3C_2Br_2$ | −8.42 | 3.07 | 0.004 | 2.117 | 2.626 | 2.621 |
| $MoSe_2/Ti_3C_2S_2$ | −3.55 | 3.03 | 0.003 | 2.193 | 2.501 | 2.403 |
| $MoSe_2/Ti_3C_2Se_2$ | −4.82 | 3.00 | 0.000 | 2.170 | 2.628 | 2.542 |
| $MoSe_2/Ti_3C_2Cl_2$ | −3.12 | 3.14 | 0.003 | 2.120 | 2.509 | 2.506 |
| $MoSe_2/Ti_3C_2Br_2$ | −8.41 | 2.99 | 0.001 | 2.127 | 2.638 | 2.617 |

It can also be seen from Table 3 that in $MoS_2/Ti_3C_2X_2$ and $MoSe_2/Ti_3C_2X_2$, the surface functional group of monolayer $Ti_3C_2$ caused an increase in the Ti–C bond length ($d_{Ti–C}$). Among them, the $d_{Ti–C}$ of the $MoSe_2/Ti_3C_2S_2$ heterostructure reached 2.193 Å, an increase of 0.136 Å from the original 2.057 Å. The Ti–C bond length $d_{Ti–C}$ of the $MoS_2/Ti_3C_2Cl_2$ heterostructure increased by 0.047 Å. The bond lengths between Ti(1) and X in the top layer of $Ti_3C_2X_2$ were almost the same as those between Ti(2) and X in the bottom layer of $Ti_3C_2X_2$, which means that the stacking of $MoS_2$ and $MoSe_2$ in these heterostructures hardly changes the spatial structure of $Ti_3C_2X_2$. The strong coupling between the $Ti_3C_2$ and TMD interface was weakened by the functional group (S, Se, Cl, Br). The value of $d_{56}$ was defined as Mo–Se(1) minus Mo–Se(2) or Mo–S(1) minus Mo–S(2) in TMDs/$Ti_3C_2X_2$ (X = S, Se, Cl, Br). The $MoS_2/Ti_3C_2S_2$ heterostructure possessed the maximum $d_{56}$ (0.009 Å), while $d_{56}$ was zero in the $MoSe_2/Ti_3C_2Se_2$ heterostructure, indicating that the spatial structure and two-dimensional properties of the original $MoSe_2$ were well preserved. The above results show that the addition of surface functional groups can seriously weaken the electronic coupling between the monolayer TMDs and $Ti_3C_2$.

### *3.2. Electronic Properties of the TMDs/$Ti_3C_2X_2$ Heterostructures*

To investigate the electronic properties of the TMDs/$Ti_3C_2$ heterostructures, we choose the most stable configurations of ZM_SA and SA_ZM to further study the electronic properties of $MoS_2/Ti_3C_2X_2$ and $MoSe_2/Ti_3C_2X_2$, respectively. The energy band structures and density of states of the $MoS_2/Ti_3C_2$ heterostructure are presented in Figure 3. The Fermi energy level is set at zero energy. From Figure 3a, it can be seen that some energy bands cross the Fermi energy level, indicating the metallic nature of the $MoS_2/Ti_3C_2$ heterostructure. Because of a strongly coupled interaction between the $MoS_2$ and $Ti_3C_2$ monolayer, the energy bands have been hybridized severely. The total and partial density of states of the $MoS_2/Ti_3C_2$ heterostructure is shown in Figure 3b; it can be seen that the energy band near the Fermi level is mainly dominated by the 3*d* orbit of the Ti atom and the 4*d* orbit of the Mo atom. Remarkably, the electrons of the S 3*p* orbit in the conduction band are unusually more than that of the Ti 3*p* orbit. Therefore, the conduction band is mainly contributed by the Mo 4*d*, S 3*p*, and Ti 3*d* orbitals. The energy band structures and density of states of the $MoSe_2/Ti_3C_2$ heterostructure are presented in Figure 4. We note that the energy band of the $MoSe_2/Ti_3C_2$ heterostructure (see Figure 4a) has no obvious hybridization around the Fermi level, which is different from the $MoS_2/Ti_3C_2$ heterostructure. Compared with $MoS_2/Ti_3C_2$, $MoSe_2/Ti_3C_2$ has more concentrated energy bands, leading to a decrease in conductivity. The total and partial density of states of the

$MoSe_2/Ti_3C_2$ heterostructure is shown in Figure 4b; we know that the energy bands near the Fermi energy level are dominated by Ti 3*d* and Mo 4*d* orbitals. The Ti 3*p* orbital and C 2*p* orbital make a slight contribution near the Fermi energy level. The conduction band is mainly formed by Ti 3*d* and Mo 4*d* orbitals, while the valence band is formed by C 2*p*, Ti 3*d*, and Mo 4*d* orbitals, and the C 2*p* orbital plays a dominant role in the $MoSe_2/Ti_3C_2$ heterostructure. Finally, by comparing the density of states of $MoS_2/Ti_3C_2$ with that of the $MoSe_2/Ti_3C_2$ heterostructure, we find that the peak of Ti 3*d* and Mo 4*d* in the $MoS_2/Ti_3C_2$ heterostructure moves towards a higher energy level.

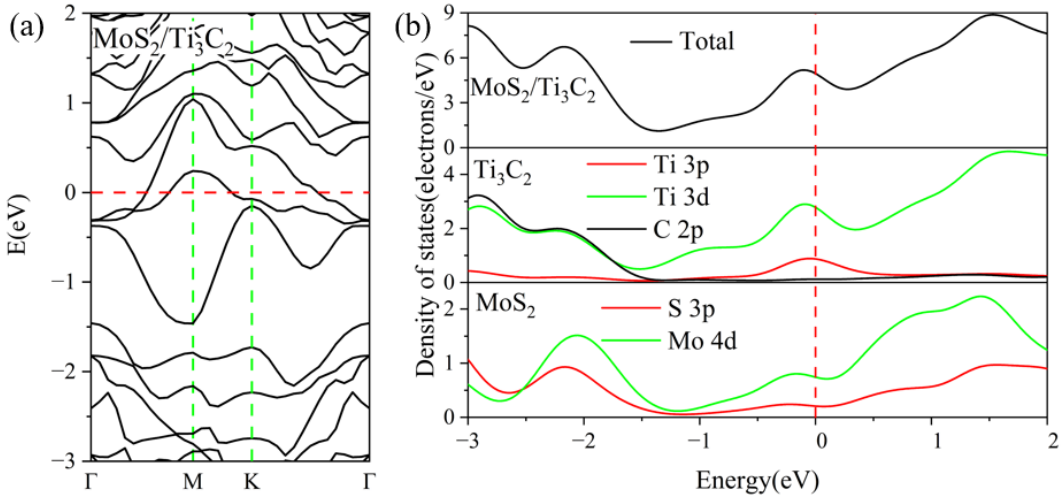


**Figure 3.** (**a**) the band structure, and (**b**) the total and partial density of states of $MoS_2/Ti_3C_2$. The Fermi level is set to 0 eV.

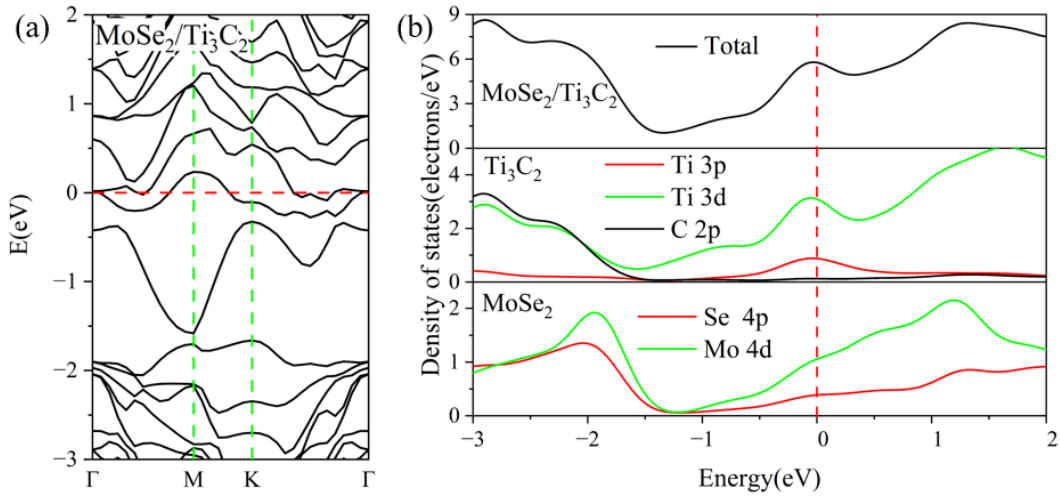


**Figure 4.** (**a**) the band structure, and (**b**) the total and partial density of states of $MoSe_2/Ti_3C_2$. The Fermi level is set to 0 eV.

It is well known that both $MoS_2$ and $MoSe_2$ are semiconductors in nature and exhibit a direct band gap at the K point in the Brillouin zone [52]. However, our calculations show that the S 3*p* orbitals, the Se 4*p* orbitals, and the Mo 4*d* orbitals in the TMDs/$Ti_3C_2$ heterostructure have a large number of electrons crossing the Fermi energy level, which is sufficient to indicate that $Ti_3C_2$ induces a significant change in the electronic properties of the TMDs monolayer.

To further understand the electronic properties, the Mulliken charge and bond populations of TMDs/$Ti_3C_2$ were calculated; see Tables S2 and S3. The interlayer electron coupling of the $MoS_2/Ti_3C_2$ heterostructure is strong due to the overlap of electron clouds

between $MoS_2$ and $Ti_3C_2$ (the bond population of the S–Ti bond is 0.48 Å). The $Ti_3C_2$ in the $MoS_2/Ti_3C_2$ heterostructure obtains 0.06 *e* from the upper $MoS_2$ layer, and the Ti atom in $Ti_3C_2$ loses 1.55 *e*, and 1.50 *e* of Ti is transferred to the C atom. The bonding behavior of the $MoS_2/Ti_3C_2$ heterostructure is covalent in nature, as indicated by the bond populations. For $MoSe_2/Ti_3C_2$, the bond population of the Se–Ti bond has a large negative value (−0.83 Å), suggesting a weak van der Waals interaction between $MoSe_2$ and $Ti_3C_2$. According to the positive and negative values of the bond population, we can conclude that the bonding behavior in the $MoSe_2/Ti_3C_2$ heterostructure is a combination of covalent and ionic bonds.

The Mulliken charge analysis shows that more electrons are transferring from $Ti_3C_2$ to $MoS_2$ in the $MoS_2/Ti_3C_2$ heterostructure. We also noted that the Mo atom in $MoSe_2/Ti_3C_2$ and $MoS_2/Ti_3C_2$ obtains 0.35*e* and 0.01*e*, respectively. Moreover, the partial density of states in Figures 3b and 4b shows that the density of the electrons of the Mo 4*d* orbital in the $MoSe_2/Ti_3C_2$ heterostructure at the Fermi energy level is much higher than that in the $MoS_2/Ti_3C_2$ heterostructure. As a result, the Mo 4*d* orbital in $MoSe_2/Ti_3C_2$ obtains more electrons from other atoms than that in $MoS_2/Ti_3C_2$.

The electronic properties of these heterostructures were affected by the surface termination atoms of $Ti_3C_2$, as illustrated in Figures 5 and 6. Compared with $MoS_2/Ti_3C_2$ and $MoSe_2/Ti_3C_2$, the electronic properties of $MoS_2/Ti_3C_2X_2$ and $MoSe_2/Ti_3C_2X_2$ were obviously different. Although TMDs/$Ti_3C_2X_2$ heterostructures still exhibited metallic behavior, the peak values of density of states (DOS) at the Fermi level were lower than those of TMDs/$Ti_3C_2$ heterostructures. Based on our calculated DOS, it is worth noting that $MoS_2$ and $MoSe_2$ retained the semiconductor nature in the TMDs/$Ti_3C_2X_2$ heterostructures. This means that the presence of surface functional groups (Cl, Br, S, Se) weakened the interaction strength between TMDs and $Ti_3C_2$. Compared with the DOS of the original monolayer $MoS_2$ and $MoSe_2$, see Figures S2 and S3, that of $MoS_2$ and $MoSe_2$ in $MoS_2/Ti_3C_2Br_2$ and $MoS_2/Ti_3C_2Cl_2$ showed an upward shift of the Fermi energy level. From the partial density of states (PDOS) of $MoS_2/Ti_3C_2Br_2$ and $MoS_2/Ti_3C_2Cl_2$, it can be seen that the energy band near the Fermi level was mainly contributed to by the Ti 3*d* orbit. The Mo atom 4*d* orbital in $MoS_2/Ti_3C_2Br_2$ made a small charge contribution, while the Mo atom 4*d* orbital in $MoS_2/Ti_3C_2Cl_2$ made almost no charge contribution to the Fermi level. In addition, the atoms of the functional groups Cl and Br made almost no contribution near the Fermi level, as shown in Figure 5a,b. When the $Ti_3C_2$ surface was terminated by S and Se functional groups, the DOS of $MoS_2$ and $MoSe_2$ showed a downward shift of the Fermi level, while the S 3*p* and Se 4*p* orbitals made an obvious charge contribution near the Fermi level. The energy band near the Fermi level became flatter, and the effective mass of the electron was larger, so the conductivity decreased. It can be seen from the density of states of $Ti_3C_2X_2$ (X = S, Se) that the S 3*p* and Se 4*p* orbital charges and Ti 3*d* orbital generated strong hybridization, respectively, as shown in Figure 5c,d. The metal behavior of the $MoS_2/Ti_3C_2X_2$ (X = Br, Cl, S, Se) heterostructure was mainly dominated by the Ti 3*d* orbital charge.

Figure 6a shows the energy band and density of states of the $MoSe_2/Ti_3C_2Br_2$ heterostructure. The bottom of the conduction band of $MoSe_2$ moved downward and coincides with the Fermi level. At the Fermi energy level, only the Ti 3*d* orbital charge contributed. For $MoSe_2/Ti_3C_2Cl_2$ and $MoSe_2/Ti_3C_2S_2$, as shown in Figure 6b,c, the Fermi energy level was located between the top of the valence band and the bottom of the conduction band. The Ti 3*d* orbital dominated the metal properties of $MoSe_2/Ti_3C_2Cl_2$ and $MoSe_2/Ti_3C_2S_2$. For $MoSe_2/Ti_3C_2Se_2$, as shown in Figure 6d, the energy band structure of $MoSe_2$ remained unchanged, and the Fermi level was located at the top of the valence band. The Se 4*p* and Ti 3*d* orbitals in $Ti_3C_2Se_2$ generate strong hybridization, which dominated the conductivity of $MoSe_2/Ti_3C_2Se_2$. Moreover, the PDOS of $MoSe_2$ and $MoS_2$ showed that both S 3*p* orbitals in $MoS_2$ and Se 4*p* orbitals in $MoSe_2$ made no charge contribution at the Fermi energy level. When S and Se were used as the functional group terminal in $Ti_3C_2$, the S 3*p* and Se 4*p* orbital charges played a leading role in the Fermi energy level.

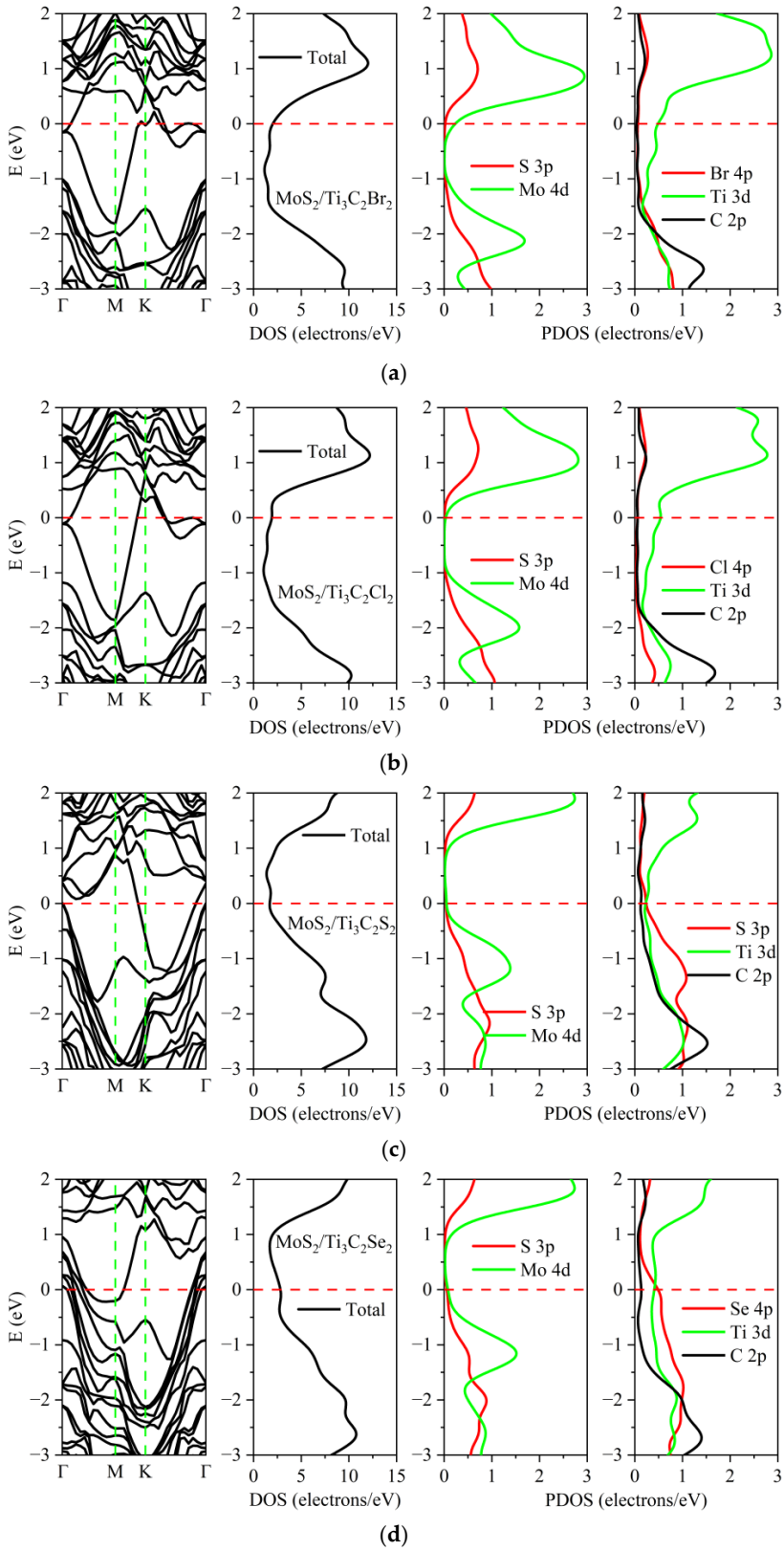


**Figure 5.** Band structures and densities of states of the $MoS_2/Ti_3C_2$ heterostructure with different terminated groups: (**a**) -Br, (**b**) -Cl, (**c**) -S and (**d**) -Se. The Fermi level is set to 0 eV. The vertical dashed line gives the location of the Fermi level. The red line represents the Fermi level. The green line represents the high symmetry point of the Brillouin zone.

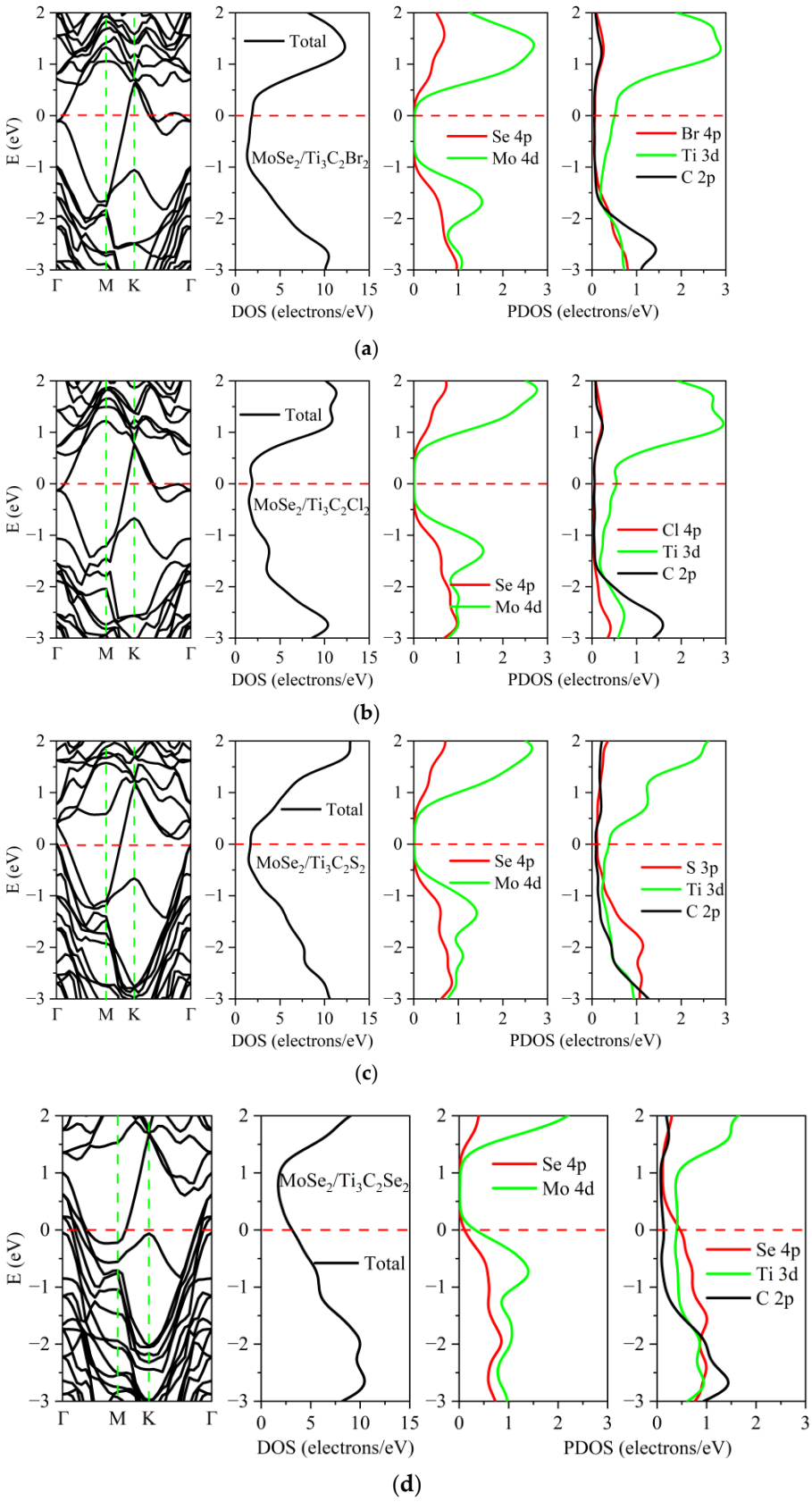


**Figure 6.** Band structures and densities of states of the $MoSe_2/Ti_3C_2$ heterostructure with different terminated groups: (**a**) -Br, (**b**) -Cl, (**c**) -S and (**d**) -Se. The Fermi level is set to 0 eV. The vertical dashed line gives the location of the Fermi level.

### *3.3. Effect of Biaxial Strain on the Structural and Electronic Properties of the TMDs/$Ti_3C_2$ Heterostructures*

Strain can be used to tune the electronic properties of two-dimensional materials [53,54]. Here, we systematically investigated the effect of biaxial strain on the structural and electronic properties of TMDs/$Ti_3C_2$ and TMDs/$Ti_3C_2X_2$. Considering a series of biaxial tensile or compressive strains $\varepsilon$ in 0.01 steps from −9% to +9%, $\varepsilon > 0$ and $\varepsilon < 0$ represented the tensile and compressive strains, respectively. Figure 7a shows the variation curve of the $MoS_2/Ti_3C_2$ interlayer distance with biaxial tensile (compressive) strain. It can be seen that the interlayer distance *d* of the $MoS_2/Ti_3C_2$ heterostructure varies linearly with an increasing biaxial tensile or compressive strain. The interlayer distance of $MoS_2/Ti_3C_2$ decreases to 1.56 Å when the biaxial tensile strain reaches 9%. Therefore, the biaxial tensile strain can enhance the electronic coupling strength between the monolayer $MoS_2$ and $Ti_3C_2$. However, its interlayer distance gradually increases when subjected to biaxial compressive strain, and the interlayer distance increased to 1.89 Å at 9% compressive strain, indicating that the electron coupling strength between the monolayer $MoS_2$ and $Ti_3C_2$ is severely weakened by the biaxial compressive strain. Figure 7b presents the variation curve of the $MoSe_2/Ti_3C_2$ interlayer distance with the biaxial tensile (compressive) strain. The result is completely different to that of the $MoS_2/Ti_3C_2$ heterostructure. The interlayer distance of the $MoSe_2/Ti_3C_2$ heterostructure shows a fluctuating change with an increasing biaxial tensile or compressive strain. Based on the above Mulliken charge and bond populations analysis of $MoS_2/Ti_3C_2$ and $MoSe_2/Ti_3C_2$, it can be seen that the bond population of S–Ti in $MoS_2/Ti_3C_2$ is positive, while that of Se–Ti in $MoSe_2/Ti_3C_2$ is negative. Therefore, the reason may be that the $MoSe_2/Ti_3C_2$ heterostructure has van der Waals interactions rather than strong electron coupling interactions.

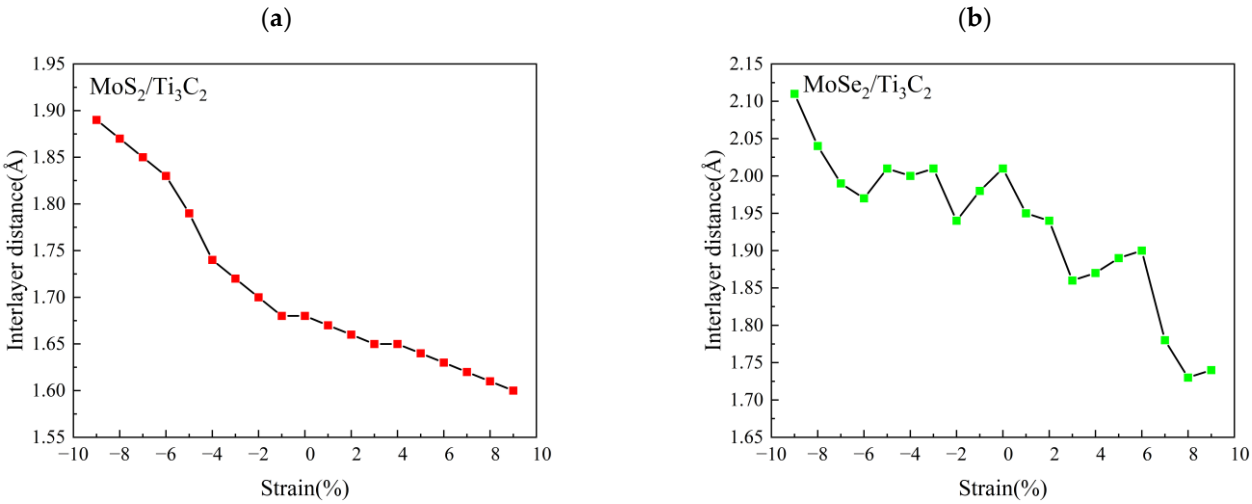


**Figure 7.** (**a**) Relationship curve between $MoS_2/Ti_3C_2$ interlayer distance and biaxial strain, (**b**) Relationship curve between $MoSe_2/Ti_3C_2$ interlayer distance and biaxial strain.

We further investigated the effect of the biaxial tensile and compressive strain on the interlayer distance *d* of TMDs/$Ti_3C_2X_2$ heterostructures; see Figure 8. It can be seen that under the condition of the applied strain, the interlayer distance of TMDs/$Ti_3C_2X_2$ heterostructures presents a completely different behavior to that of $MoS_2/Ti_3C_2$. The reason is the different electronic coupling strength between the monolayer TMDs and $Ti_3C_2X_2$ due to the surface functional groups. The interlayer distance between $MoS_2$ and $Ti_3C_2Cl_2$ remains almost unchanged under the compressive strain, while it increases slightly with the increase in the tensile strain, as shown in Figure 8a. The interlayer distance of $MoS_2/Ti_3C_2S_2$ heterostructures presents a steady increase under tensile strain. When the compressive strain is in the range from 0 to 5%, its interlayer distance rapidly increases; when the compressive strain is above 5%, its interlayer distance is almost unchanged.

For the $MoS_2/Ti_3C_2Br_2$ heterostructure, under the condition of compressive or tensile strain, the coupling strength between valence electrons of Br atoms and the 4*d* orbital of Mo atoms is weakened. As a result, the interlayer distance between $MoS_2$ and $Ti_3C_2Br_2$ increases slightly with the increase in the applied strain. Compared with $MoS_2/Ti_3C_2X_2$ (X = S, Br, Cl), the interlayer distance of $MoS_2/Ti_3C_2Se_2$ presents a significantly fluctuating change in the case of compressive strain. The reason may be that the Se atom induces the aberration of a crystal lattice due to its larger atomic radii [35]. When the compressive strain is applied, the lattice distortion becomes more pronounced, resulting in the fluctuation of the interlayer distance. For $MoSe_2/Ti_3C_2X_2$ (X = S, Se, Cl, Br), we also observed a similar trend under the condition of compressive strain; see Figure 8b. Therefore, we concluded that the fluctuation in the interlayer distance in $MoS_2/Ti_3C_2X_2$ (X = Se) and $MoSe_2/Ti_3C_2X_2$ is mainly attributed to the existence of the Se atom, and the displacement of the Se atom affects the structural stability of these heterostructures.

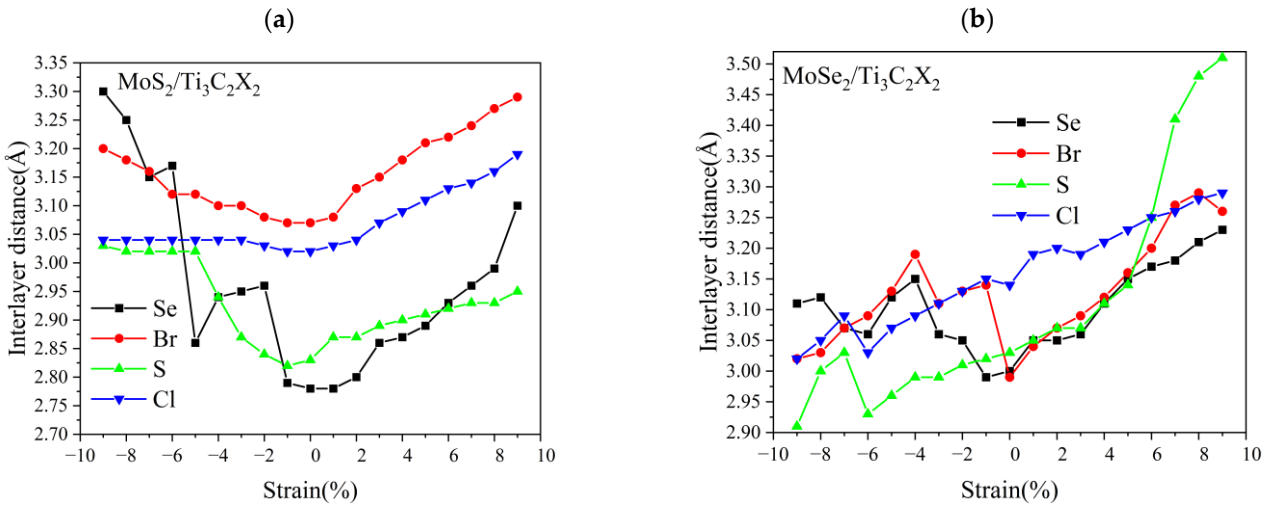


**Figure 8.** (**a**) Relationship curve between $MoS_2/Ti_3C_2X_2$ (X = Se, Br, S, Cl) interlayer distance and biaxial strain, (**b**) Relationship curve between $MoSe_2/Ti_3C_2X_2$ (X = Se, Br, S, Cl) interlayer distance and biaxial strain.

Figure 8b shows that the interlayer distance of $MoSe_2/Ti_3C_2X_2$ dramatically increases with the increase in the tensile strain, and the interlayer distances of $MoSe_2/Ti_3C_2Se_2$ and $MoSe_2/Ti_3C_2Br_2$ at 9% tensile strain increase to 3.23 Å and 3.26 Å, respectively. Under the compressive strain, their interlayer distance increases nonlinearly. Therefore, the applied strain weakened the interlayer interaction between $MoSe_2$ and $Ti_3C_2X_2$ (X = Se, Br). For $MoSe_2/Ti_3C_2S_2$ and $MoSe_2/Ti_3C_2Cl_2$, their interlayer distance presents the same trend under the applied strain. Under the tensile strain, the interlayer distance increases, while under the compressive strain, the interlayer distance becomes increasingly smaller. Moreover, the interlayer distance of $MoSe_2/Ti_3C_2S_2$ is more sensitive to the applied strain than that of $MoSe_2/Ti_3C_2Cl_2$. It is noted that the interlayer distance of $MoSe_2/Ti_3C_2S_2$ increased to 3.52 Å at 9% tensile strain, in contrast; its interlayer distance decreased to 2.91 Å at 9% compressive strain.

To explore the effect of biaxial strain on the electronic properties of TMDs/$Ti_3C_2$ heterostructures, we first investigated the Mulliken charge of TMD/$Ti_3C_2$ heterostructure under tensile and compressive strain. Table 4 shows the Mulliken charge population of $MoS_2/Ti_3C_2$ heterostructures, at free strain, $Ti_3C_2$ loses 0.07*e*, which is transferred to the monolayer $MoS_2$. At a tensile strain of 9%, $Ti_3C_2$ loses more electrons (0.11*e*). Moreover, Mo atoms also lose 0.05 electrons when subjected to tensile strain. At a compressive strain of 9%, $Ti_3C_2$ loses fewer electrons (0.03*e*). Table 5 shows the Mulliken charge population of $MoSe_2/Ti_3C_2$ heterostructures. At a compressive strain of 9%, $MoSe_2$ loses more electrons (0.08*e*), which are transferred to $Ti_3C_2$. These results showed that the interlayer electron

transfer in both $MoS_2/Ti_3C_2$ and $MoSe_2/Ti_3C_2$ can be well regulated by biaxial strain. The difference is that in the $MoS_2/Ti_3C_2$ heterostructure the electrons are transferred from $Ti_3C_2$ to $MoS_2$, while in the $MoSe_2/Ti_3C_2$ heterostructure, the electrons are transferred from $MoSe_2$ to $Ti_3C_2$. Moreover, in the $MoS_2/Ti_3C_2$ heterostructure the transferring electrons increase with increasing tensile strain, while in the $MoSe_2/Ti_3C_2$ heterostructure, they increase with increasing compressive strain.

**Table 4.** Mulliken charge (electron) of $MoS_2/Ti_3C_2$.

| Species | Ion | Total | Charge | Total | Charge | Total | Charge |
|---|---|---|---|---|---|---|---|
| | | **Compressive 9%** | | **Strain Free** | | **Tensile 9%** | |
| C | 1 | 4.70 | −0.70 | 4.75 | −0.75 | 4.78 | −0.78 |
| C | 2 | 4.69 | −0.69 | 4.71 | −0.71 | 4.71 | −0.71 |
| S | 1 | 5.94 | 0.06 | 5.98 | 0.02 | 6.05 | −0.05 |
| S | 2 | 6.01 | −0.01 | 6.06 | −0.06 | 6.11 | −0.11 |
| Ti | 1 | 11.24 | 0.76 | 11.25 | 0.75 | 11.34 | 0.66 |
| Ti | 2 | 11.62 | 0.38 | 11.59 | 0.41 | 11.57 | 0.43 |
| Ti | 3 | 11.72 | 0.28 | 11.63 | 0.37 | 11.49 | 0.51 |
| Mo | 1 | 14.08 | −0.08 | 14.03 | −0.03 | 13.95 | 0.05 |

**Table 5.** Mulliken charge (electron) of $MoSe_2/Ti_3C_2$.

| Species | Ion | Total | Charge | Total | Charge | Total | Charge |
|---|---|---|---|---|---|---|---|
| | | **Compressive 9%** | | **Strain Free** | | **Tensile 9%** | |
| C | 1 | 4.69 | −0.69 | 4.71 | −0.71 | 4.71 | −0.71 |
| C | 2 | 4.70 | −0.70 | 4.75 | −0.75 | 4.78 | −0.78 |
| Se | 1 | 5.87 | 0.13 | 5.86 | 0.14 | 5.90 | 0.10 |
| Se | 2 | 5.68 | 0.32 | 5.77 | 0.23 | 5.74 | 0.26 |
| Ti | 1 | 11.27 | 0.73 | 11.27 | 0.73 | 11.36 | 0.64 |
| Ti | 2 | 11.71 | 0.29 | 11.62 | 0.38 | 11.49 | 0.51 |
| Ti | 3 | 11.71 | 0.29 | 11.67 | 0.33 | 11.69 | 0.31 |
| Mo | 1 | 14.37 | −0.37 | 14.35 | −0.35 | 14.33 | −0.33 |

To further investigate the effect of biaxial strain on the electronic properties of TMDs/$Ti_3C_2$ heterostructures, we calculated their energy band structures and density of states under different strains. Figure 9a presents the energy band structures of $MoS_2/Ti_3C_2$ heterostructures under compressive strain. As the compressive strain increased, the valence band I moved down and away from the Fermi energy level, and it became flatter and flatter. The energy bands II and III at the Γ point were split, and the energy band II became more dispersed. Moreover, the energy bands III and IV were combined, and then they moved away from the Fermi energy level with increasing compressive strain. Figure 9b shows the energy band structures of $MoS_2/Ti_3C_2$ heterostructures under tensile strain. It can be seen that the increase in the tensile strain caused the valence bands I, II, and III to move away from the Fermi energy level and become flatter. Moreover, the conduction bands IV and V moved toward the Fermi energy level, and they showed more hybridization, resulting in an increase in the conductivity of the $MoS_2/Ti_3C_2$ heterostructure [55].

Figure 10 shows the DOS of the $MoS_2/Ti_3C_2$ heterostructure under different biaxial strains. It was obvious that the Fermi energy level was dominated by Mo 4*d* and Ti 3*d* orbitals. Moreover, the contribution of the Mo 4*d* orbital to the conduction band lessened with increasing compressive strain, while the contribution of Mo 4*d* and Ti 3*d* orbitals to the valence band increased with the increasing tensile strain. It can also be seen that the peak value of Ti atoms in the range of the conduction band increased with increasing tensile strain, while the peak value of Mo atoms remained almost unchanged with increasing tensile strain. The peak value of Mo atoms in the range of the valence band increased with the tensile strain and moved toward the Fermi energy level. Based on our

calculated DOS of the $MoS_2/Ti_3C_2$ heterostructure, the interlayer interaction between the monolayer $MoS_2$ and $Ti_3C_2$ presented different behavior under tensile and compressive strain, and the interaction strength was strengthened under tensile strain, but weakened under compressive strain.

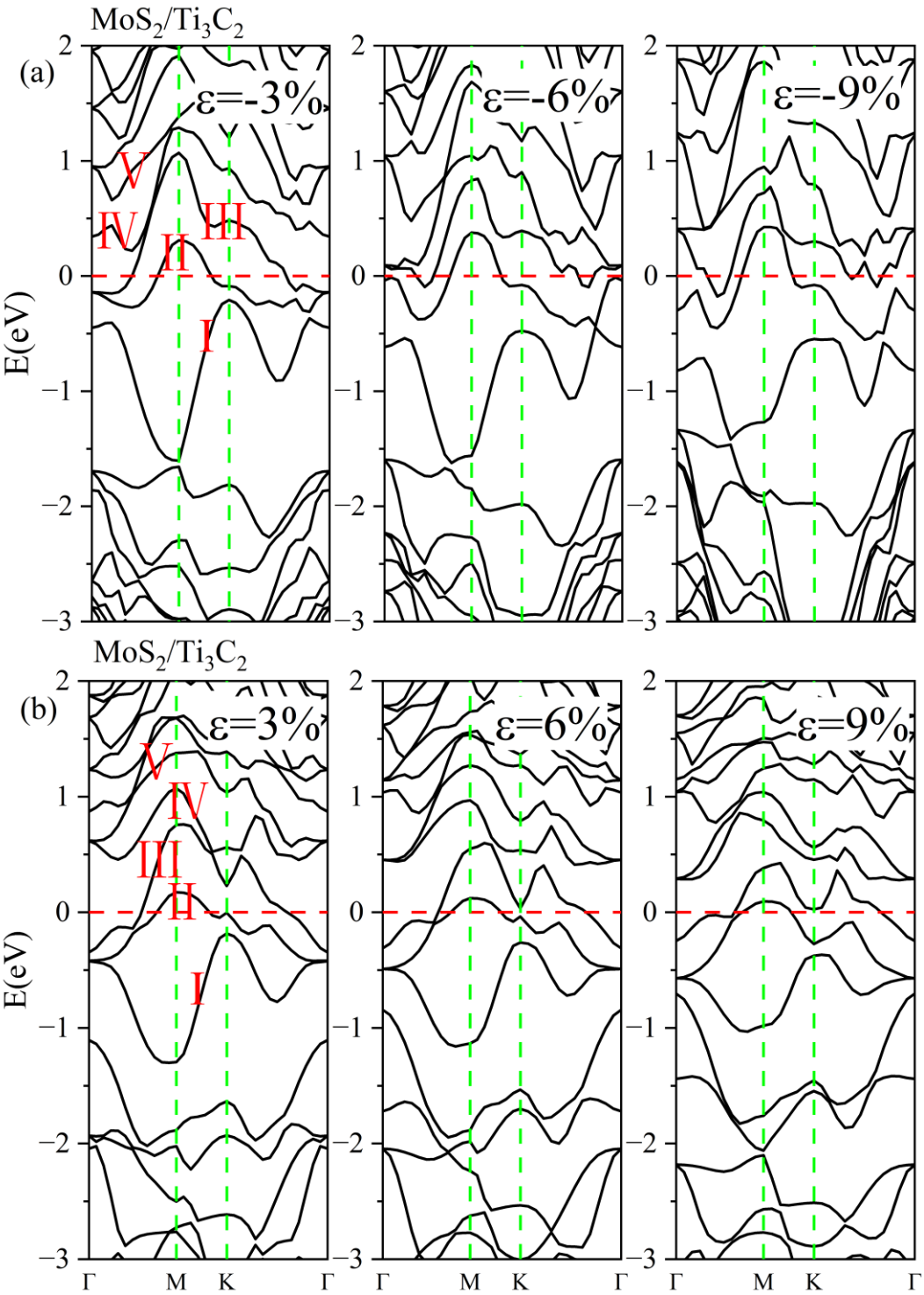


**Figure 9.** (**a**) Energy band structures of $MoS_2/Ti_3C_2$ heterostructure under different compress strains. (**b**) Energy band structures of $MoS_2/Ti_3C_2$ heterostructure under different tensile strains. The Fermi level is set to 0 eV. The red line represents the Fermi level. The green line represents the high symmetry point of the Brillouin zone. I/II/III/IV/V represents different energy bands.

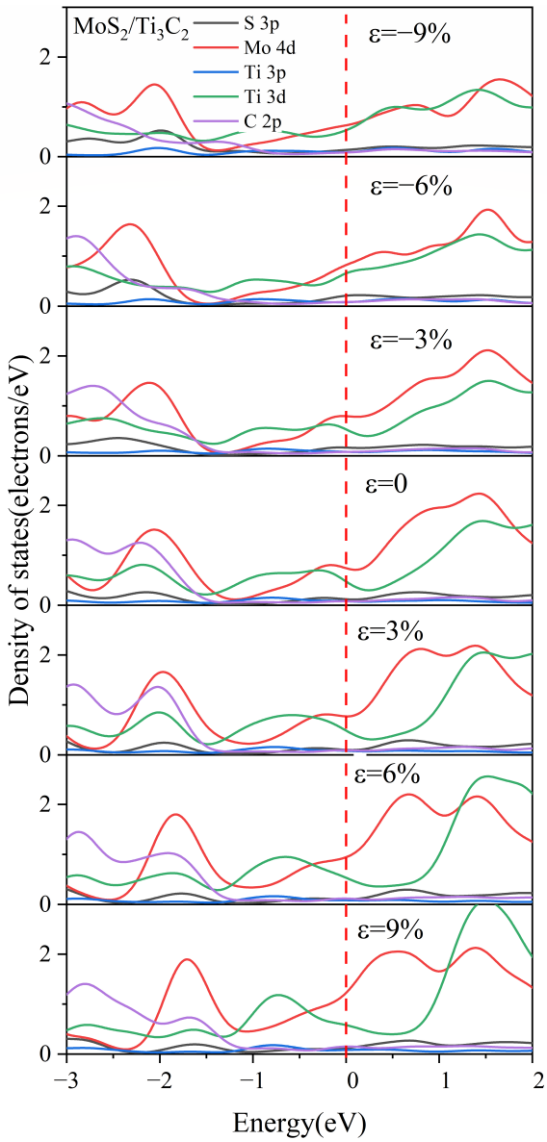


**Figure 10.** The partial density of states (PDOS) of $MoS_2$ and $Ti_3C_2$ for the $MoS_2/Ti_3C_2$ heterostructure with different biaxial strains. The Fermi level is set to 0 eV.

Figure 11a gives the energy band structures of the $MoSe_2/Ti_3C_2$ heterostructure under different compressive strains. With increasing compressive strain, the conduction bands III and IV gradually merged at the Γ point and moved away from the Fermi level. The valence band I become flatter, while the valence band II crossing the Fermi level became more tortuous, indicating a decrease in conductivity. Figure 11b displays the energy band structures of the $MoSe_2/Ti_3C_2$ heterostructure under different tensile strains. As the tensile strain increased, the energy bands II and III were split at the Γ point, and the energy bands IV and V showed more hybridization. Moreover, the energy bands crossing the Fermi energy level became more dispersed under tensile strain, inducing an increase in conductivity. We also noted that the pseudogap of the $MoSe_2/Ti_3C_2$ heterostructure disappeared with increasing compressive or tensile strain. Therefore, the applied strain can effectively tune the electronic properties of the TMDs/$Ti_3C_2$ heterostructures.

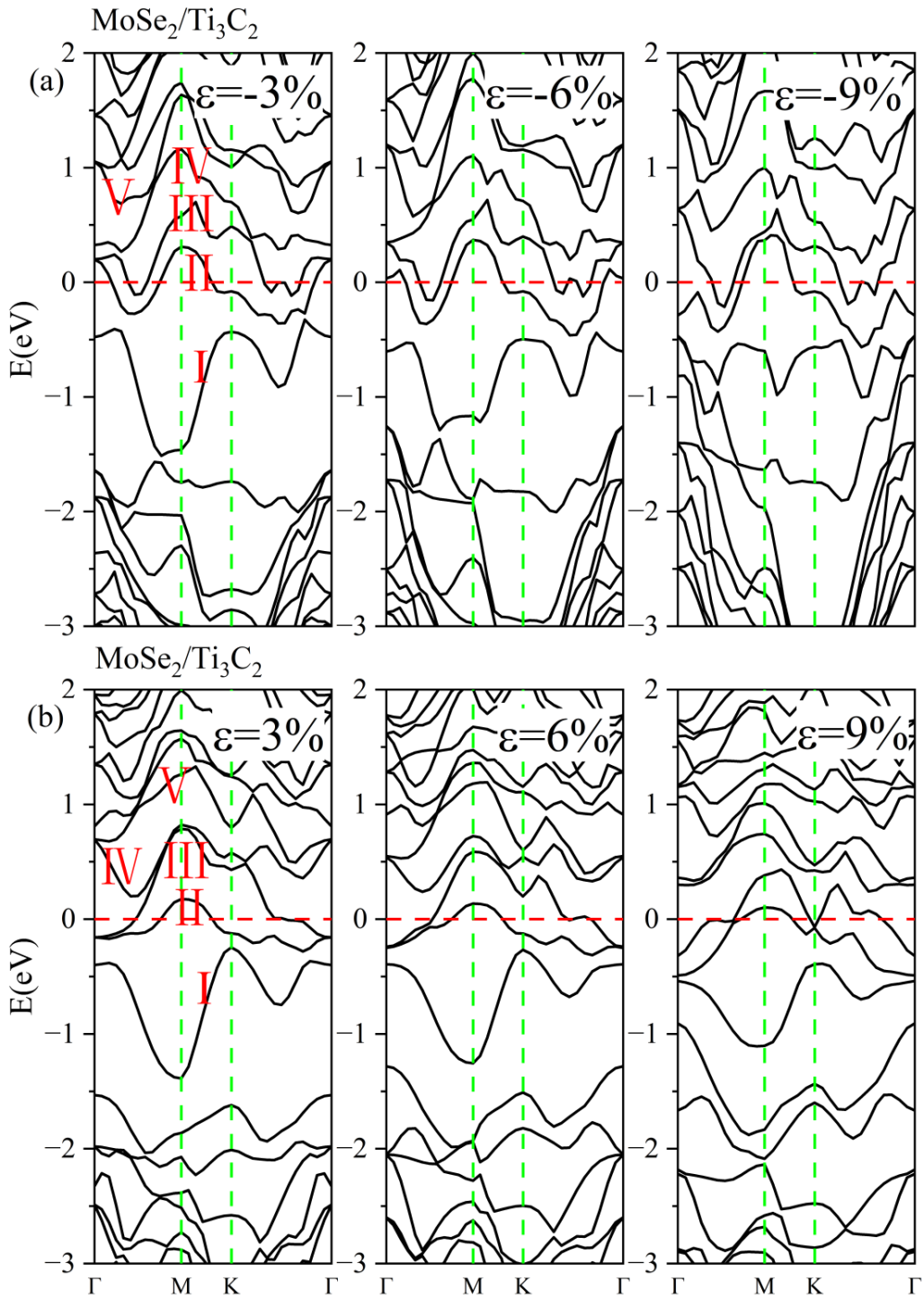


**Figure 11.** (**a**) Energy band structures of $MoSe_2/Ti_3C_2$ heterostructure under different compress strains. (**b**) Energy band structures of $MoSe_2/Ti_3C_2$ heterostructure under different tensile strains. The Fermi level is set to 0 eV. The red line represents the Fermi level. The green line represents the high symmetry point of the Brillouin zone. I/II/III/IV/V represents different energy bands.

Figure 12 illustrates the DOS of the $MoSe_2/Ti_3C_2$ heterostructure with different biaxial strains. The peak value of Mo 4*d* orbitals at −1.8 eV gradually decreased under compressive strain, while the peak value of Ti 3*d* orbitals at 0.9 eV increased with increasing compressive strain. Under tensile strain, the peak value of both the Ti 3*d* orbital at 0.9 eV and the Mo 4*d* orbital at 1.2 eV increased with increasing tensile strain. Moreover, the peak value of Ti

3*d* orbitals moved away from the Fermi level, while in contrast, the peak value of the Mo 4*d* orbitals moved toward the Fermi energy level. It can be inferred from the variation of the DOS of $MoSe_2/Ti_3C_2$ heterostructure with the strain that tensile strain increases the interlayer interaction, while compressive strain weakens the interlayer interaction. This result was consistent with the $MoS_2/Ti_3C_2$ heterostructure.

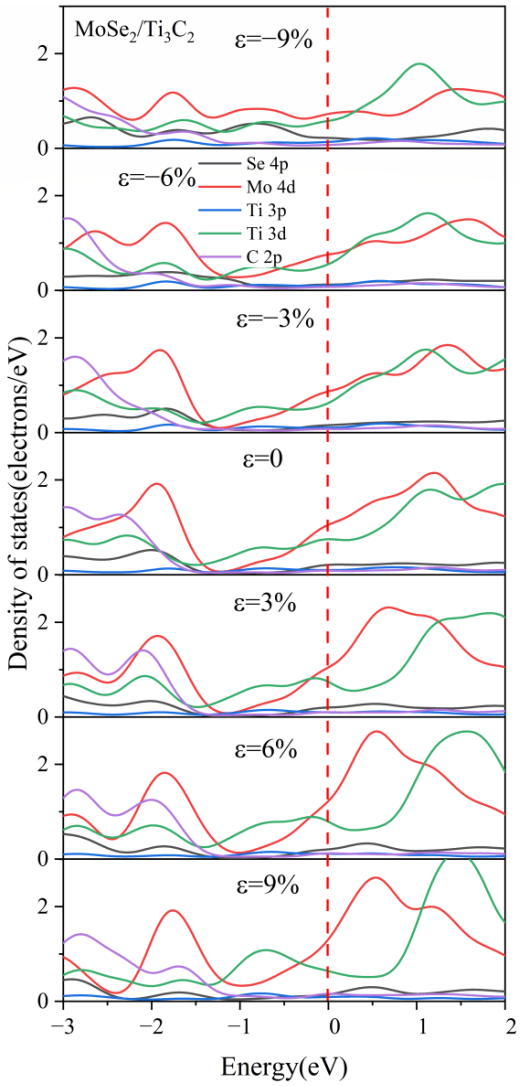


**Figure 12.** The partial density of states (PDOS) of $MoSe_2$ and $Ti_3C_2$ for the $MoSe_2/Ti_3C_2$ heterostructure with different biaxial strains. The Fermi level is set to 0 eV. The red line represents the Fermi level.

We also investigated the DOS of $MoS_2/Ti_3C_2X_2$ under different biaxial strains, as shown in Figures 13, 14, S5 and S6. Compared with $MoS_2/Ti_3C_2Se_2$ and $MoS_2/Ti_3C_2Br_2$, the external strain had a slight effect on the DOS of $MoS_2/Ti_3C_2Cl_2$ and $MoS_2/Ti_3C_2S_2$, see Figures S5 and S6. The monolayer $MoS_2$ remained in its band gap when a compressive strain was applied, while its band gap gradually disappeared with increasing tensile strain. This indicated that the tensile strain can improve the interaction strength between the monolayer $MoS_2$ and $Ti_3C_2Cl_2$ (or $Ti_3C_2S_2$). For $MoS_2/Ti_3C_2Se_2$ and $MoS_2/Ti_3C_2Br_2$, the tensile strain induced the Mo 4*d* orbital to cross the Fermi level, indicating that the semiconductor nature of the monolayer $MoS_2$ was completely destroyed. This means more electrons were transferred from the monolayer $Ti_3C_2Br_2$ (or $Ti_3C_2Se_2$) to $MoS_2$. We also noted that the S 3*p* orbital in $MoS_2/Ti_3C_2Br_2$ obviously crossed the Fermi level when the compressive strain reached 9%. In contrast, compressive strain cannot result in the S 3*p* and Mo 4*d* orbitals crossing the Fermi level in $MoS_2/Ti_3C_2Se_2$, suggesting that $MoS_2$ can

preserve its band gap under compressive strain, while the position of its conduction band minimum (CBM) and valence band maximum (VBM) will be obviously shifted.

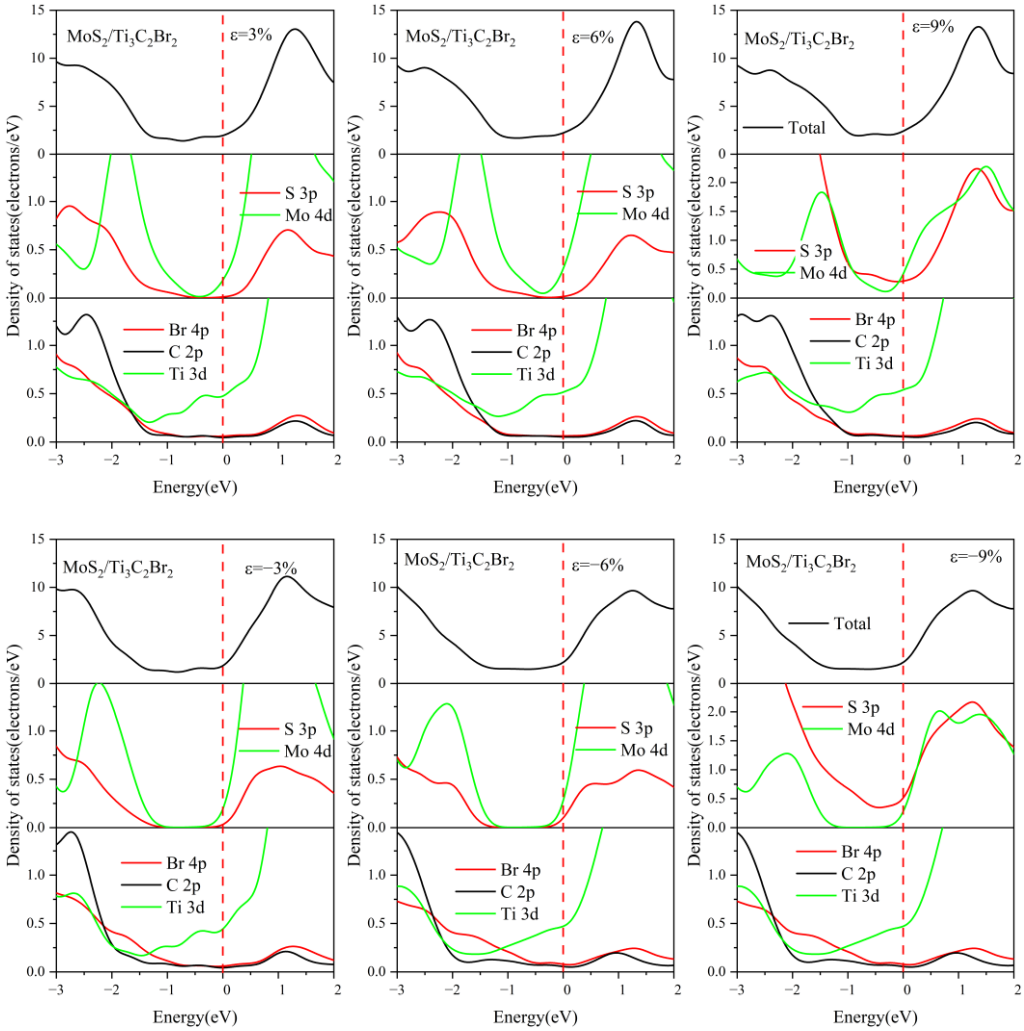


**Figure 13.** Density of states of the $MoS_2/Ti_3C_2Br_2$ heterostructure with different biaxial strains. The Fermi level is set to 0 eV.

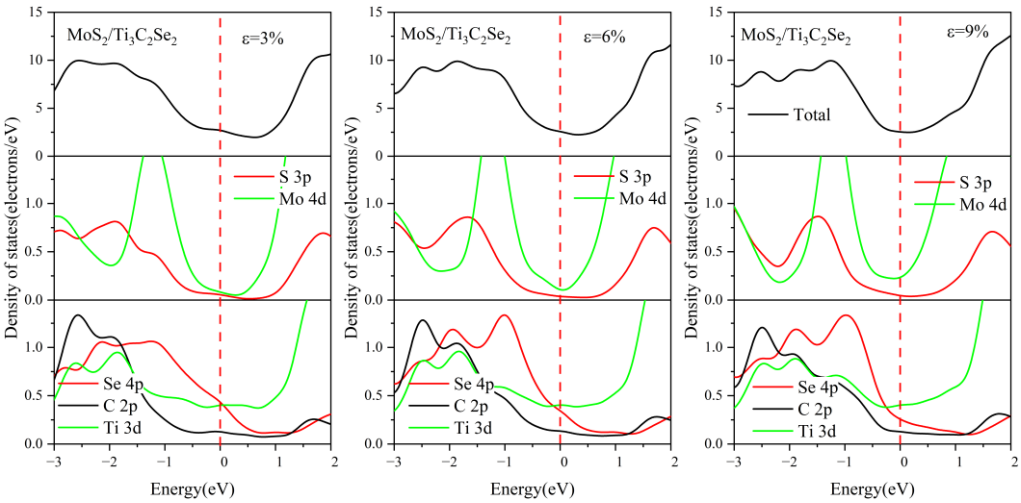


**Figure 14.** *Cont.*

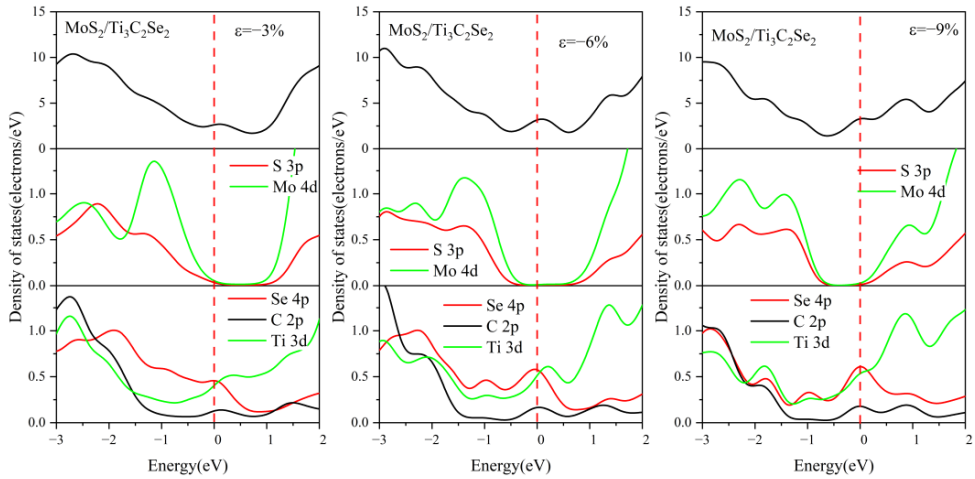


**Figure 14.** Density of states of the $MoS_2/Ti_3C_2Se_2$ heterostructure with different biaxial strains. The Fermi level is set to 0 eV.

For comparison, the DOS of $MoSe_2/Ti_3C_2X_2$ under different biaxial strains was also investigated, see Figures 15, 16, S7 and S8. For these four kinds of $MoSe_2/Ti_3C_2X_2$ heterostructures, the band gap of monolayer $MoSe_2$ disappeared with increasing compressive or tensile strain, and the Mo 4*d* orbitals and Se 4*p* orbitals passed through the Fermi energy levels. Therefore, the $MoSe_2/Ti_3C_2X_2$ heterostructure is more sensitive to external strain than the $MoS_2/Ti_3C_2X_2$ heterostructure. Moreover, these $MoSe_2/Ti_3C_2X_2$ heterostructures had a similar response to external strain. When there was no strain, the single-layer $MoSe_2$ maintained its original semiconductor properties (see Figure 6), and the Fermi energy level was at the VBM of the $MoSe_2$. When the tensile or compressive strain was above 6%, $MoSe_2$ was transformed into a conductor. The tensile and compressive strain can obviously increase the charge contribution of Mo 4*d* orbitals and Se 4*p* orbitals at the Fermi energy level. Moreover, under compressive strain, the PDOS peak value of these $MoSe_2/Ti_3C_2X_2$ heterostructures becomes sharper, indicating that the electron localization is strong.

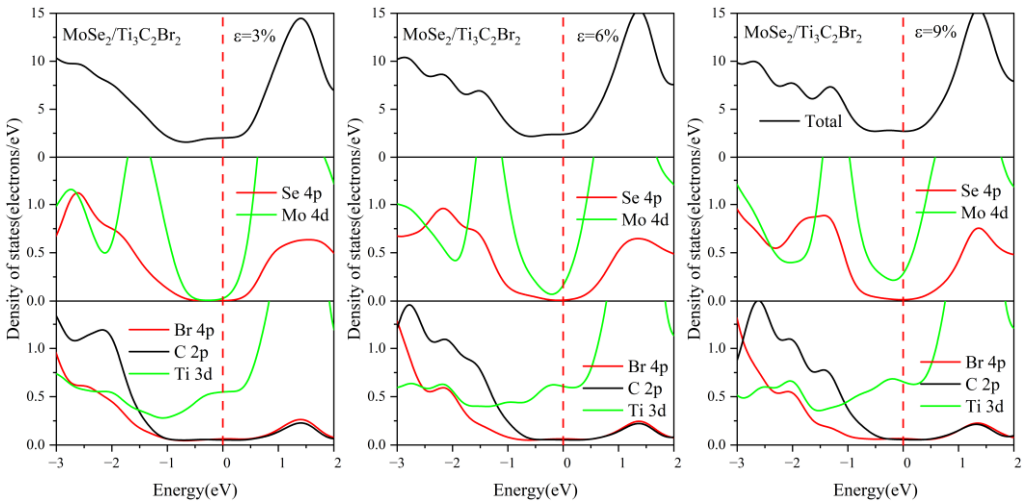


**Figure 15.** *Cont*.

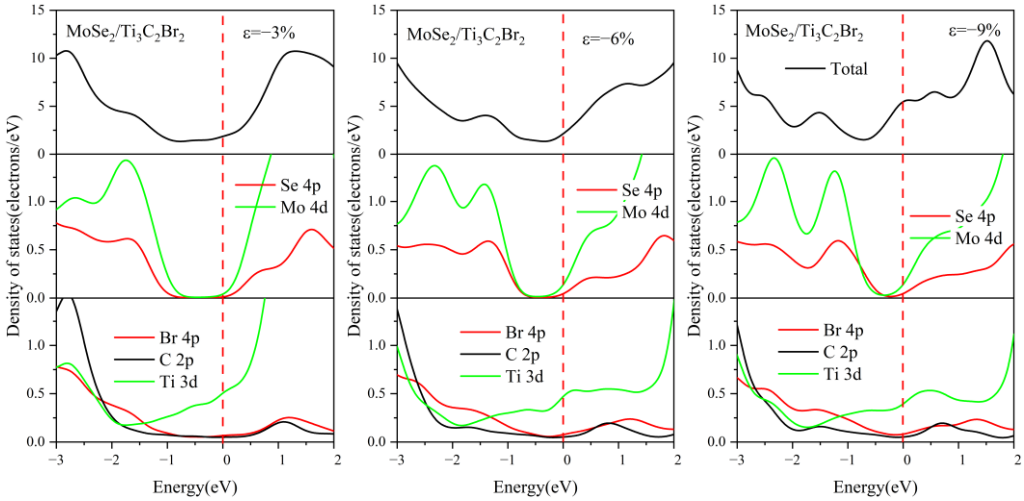


**Figure 15.** Density of states of the $MoSe_2/Ti_3C_2Br_2$ heterostructure with different biaxial strains. The Fermi level is set to 0 eV.

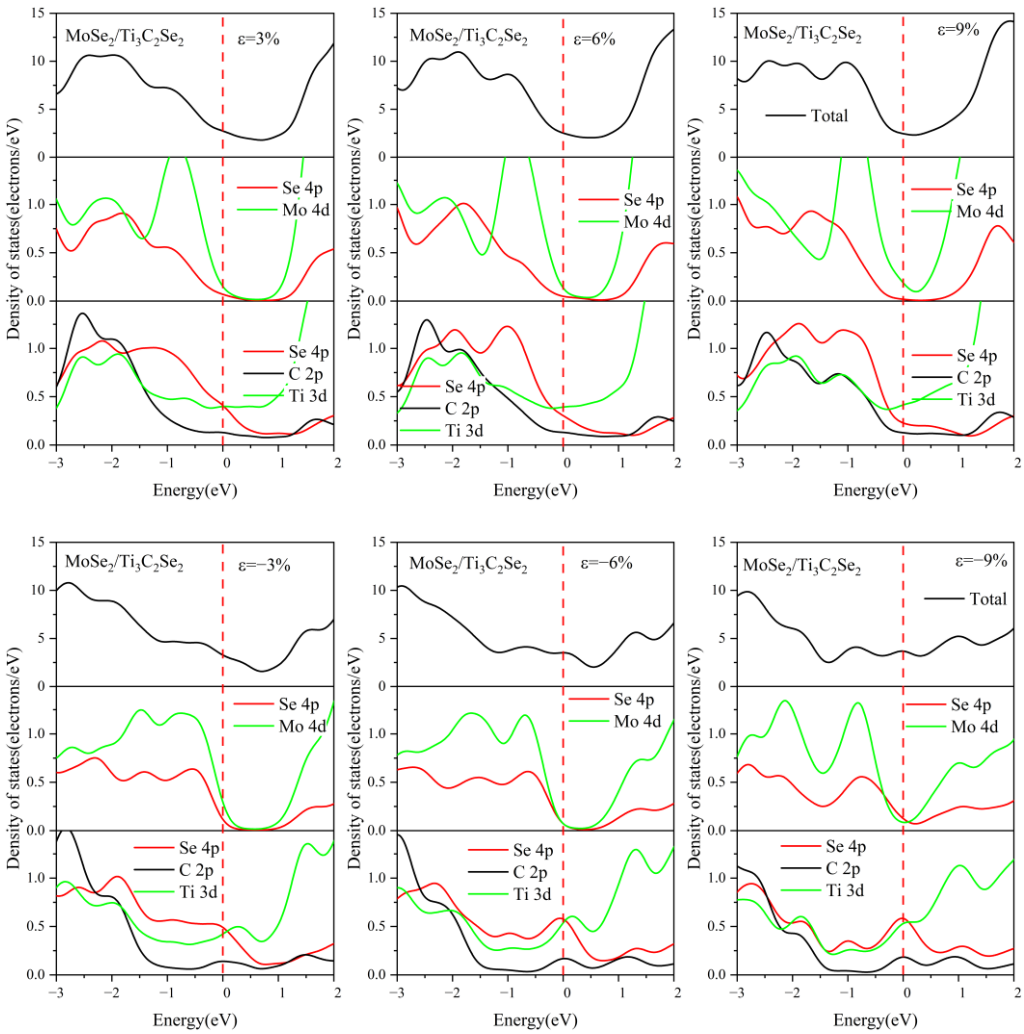


**Figure 16.** Density of states of the $MoSe_2/Ti_3C_2Se_2$ heterostructure with different biaxial strains. The Fermi level is set to 0 eV.

### 3.4. Effect of Electric Field on the Electronic Properties of the TMDs/$Ti_3C_2X_2$ Heterostructures

Some studies [56,57] have shown that the electric field is a useful way to tune the electronic properties of heterostructures. In this section, we focus on the effects of the vertical electric field on the electronic properties of TMDs/$Ti_3C_2X_2$ heterostructures. To determine the effect of different directions of the applied electric field on the electronic properties of these heterostructures, we defined that the direction of the TMDs pointing to $Ti_3C_2X_2$ was the positive direction of the applied vertical electric field, and the reverse direction was negative. The gradient from −0.9 V/Å to +0.9 V/Å for the applied electric field was taken in steps of 0.3 V/Å.

Figure 17 shows the DOS of $MoS_2/Ti_3C_2X_2$ and PDOS of $MoS_2$ in $MoS_2/Ti_3C_2X_2$ (X = S, Se, Cl, Br) under different electric fields. The monolayer $MoS_2$ maintained its band gap under the positive and negative electric fields. The position of the valence band maximum (VBM) and conduction band minimum (CBM) of $MoS_2$ in $MoS_2/Ti_3C_2Br_2$ and $MoS_2/Ti_3C_2Cl_2$ remained almost unchanged under the negative electric field. In contrast, the VBM and CBM of $MoS_2$ in $MoS_2/Ti_3C_2Br_2$ and $MoS_2/Ti_3C_2Cl_2$ underwent a significant shift under the positive electric field, and the peak of the Mo 4*d* orbital moved toward a higher energy level, as shown in Figure 17a,b. Compared with $MoS_2/Ti_3C_2Br_2$ and $MoS_2/Ti_3C_2Cl_2$, the effect of the electric field on the VBM and CBM of $MoS_2$ in $MoS_2/Ti_3C_2Se_2$ and $MoS_2/Ti_3C_2S_2$ presented a completely reverse case. The position of VBM and CBM of $MoS_2$ in $MoS_2/Ti_3C_2Se_2$ and $MoS_2/Ti_3C_2S_2$ remained almost unchanged under the positive electric field, while obviously moving under the negative electric field. Moreover, the peak position of the Mo 4*d* orbital remained almost constant, see Figure 17c,d. The DOS values of $MoSe_2$ in $MoSe_2/Ti_3C_2X_2$ (X = S, Se, Cl, Br) under different electric fields were investigated, and the results were very similar to the $MoS_2/Ti_3C_2X_2$, see Figure S4. Compared with $MoS_2/Ti_3C_2Br_2$ and $MoS_2/Ti_3C_2Se_2$, the total DOS of $MoS_2/Ti_3C_2S_2$ and $MoS_2/Ti_3C_2Cl_2$ obviously moved near the Fermi Level, suggesting the shift of VBE and CBE of $MoS_2$. Moreover, under the condition of a positive electric field, the total DOS of $MoS_2/Ti_3C_2Cl_2$ presented a sharp peak around 1 eV.

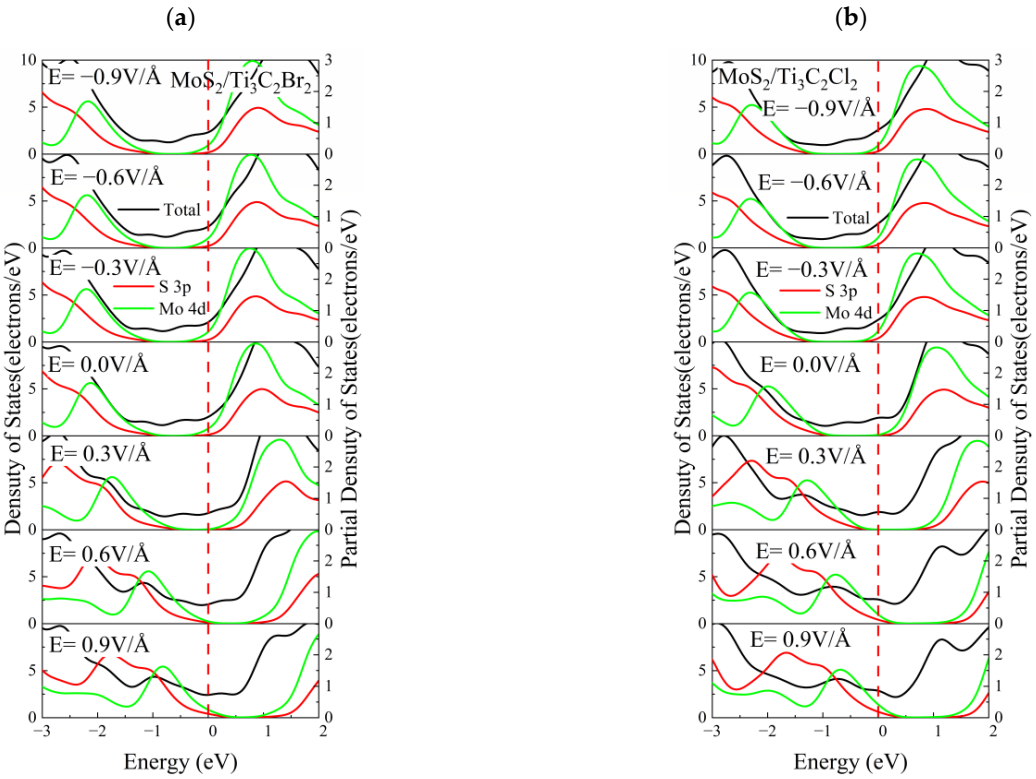


**Figure 17.** *Cont.*

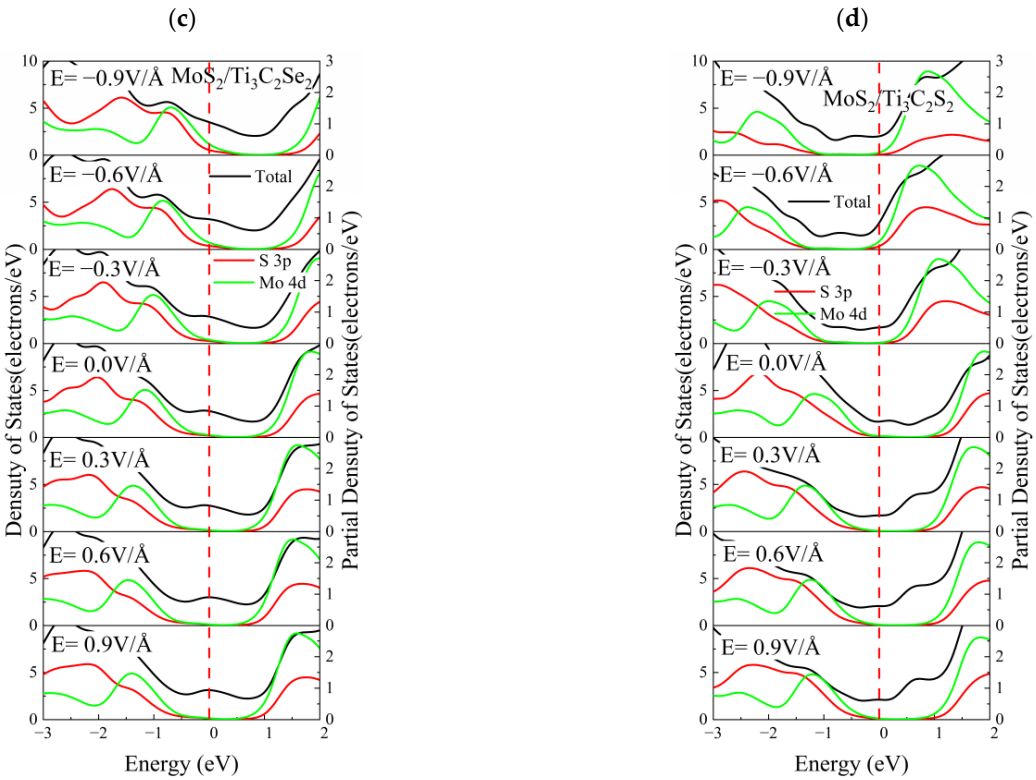


**Figure 17.** The DOS of $MoS_2/Ti_3C_2X_2$ and PDOS of $MoS_2$ in $MoS_2/Ti_3C_2X_2$ heterostructures under different electric fields. (**a**) X-Br, (**b**) X-Cl, (**c**) X-Se and (**d**) X-S.

We further analyzed the energy band structure of TMDs/$Ti_3C_2X_2$ (X = S, Se, Cl, Br) heterostructures near the Fermi energy level in the electric field range from −0.9 V/Å to 0.9 V/Å, as shown in Figure 18. Figure 18a gives the variation patterns of the energy band edges at the M and K points near the Fermi energy level for $MoS_2/Ti_3C_2X_2$ (X = Se, Br) heterostructures under different electric fields. For $MoS_2/Ti_3C_2Br_2$, the conduction band edge (CBE) and valence band edge (VBE) at both the M the K points moved towards a higher energy level with increasing electric field strength in the positive direction, while they were almost pinned under the negative electric field. In contrast, both the CBE and the VBE of $MoS_2/Ti_3C_2Se_2$ at the K point moved towards a higher energy level with increasing negative electric field strength, while the CBE at the K point under the positive electric field moved towards a lower energy level. Under the positive electric field, both the CBE and VBE of $MoS_2/Ti_3C_2Se_2$ at the M point remained unchanged. For $MoS_2/Ti_3C_2X_2$ (X = S, Cl), see Figure 18b, the VBE and CBE of $MoS_2/Ti_3C_2Cl_2$ at the M point and K point near the Fermi level were similar to those of the $MoS_2/Ti_3C_2Br_2$ heterostructure. The energy level of both the CBE and VBE of $MoS_2/Ti_3C_2S_2$ at the M point increased linearly with increasing positive electric field strength, while it decreased slightly with the negative electric field. It is worth noting that the CBE and VBE of $MoS_2/Ti_3C_2S_2$ at the K point were almost pinned under the positive and negative electric fields. For $MoSe_2/Ti_3C_2Br_2$, the energy level of the CBE and VBE at the M and K points decreased linearly with an increasing positive electric field, while it increased with an increasing negative electric field, see Figure 18c. The energy band edge of $MoSe_2/Ti_3C_2Se_2$ was almost independent of the positive and negative electric fields. From Figure 18d, we know that for $MoSe_2/Ti_3C_2S_2$ the energy level of the CBE and VBE at the K point and M point were insensitive to the external electric field. For $MoSe_2/Ti_3C_2Cl_2$, the energy level of the CBE at the K point and M point showed a slight change under the condition of the positive electric field, while it could be pinned when the negative electric field was applied. The energy level of the VBE at the K point and M point remained unchanged when the electric field strength was increased to 0.3 V/Å.

The energy band edges of TMDs/$Ti_3C_2X_2$ (X = S, Se, Cl, Br) heterostructures showed a significant change near the Fermi energy level under different directional electric fields, indicating that the combined functional group with the electric field can effectively tune the related properties of TMDs/$Ti_3C_2X_2$ (X = S, Se, Cl, Br) heterostructures.

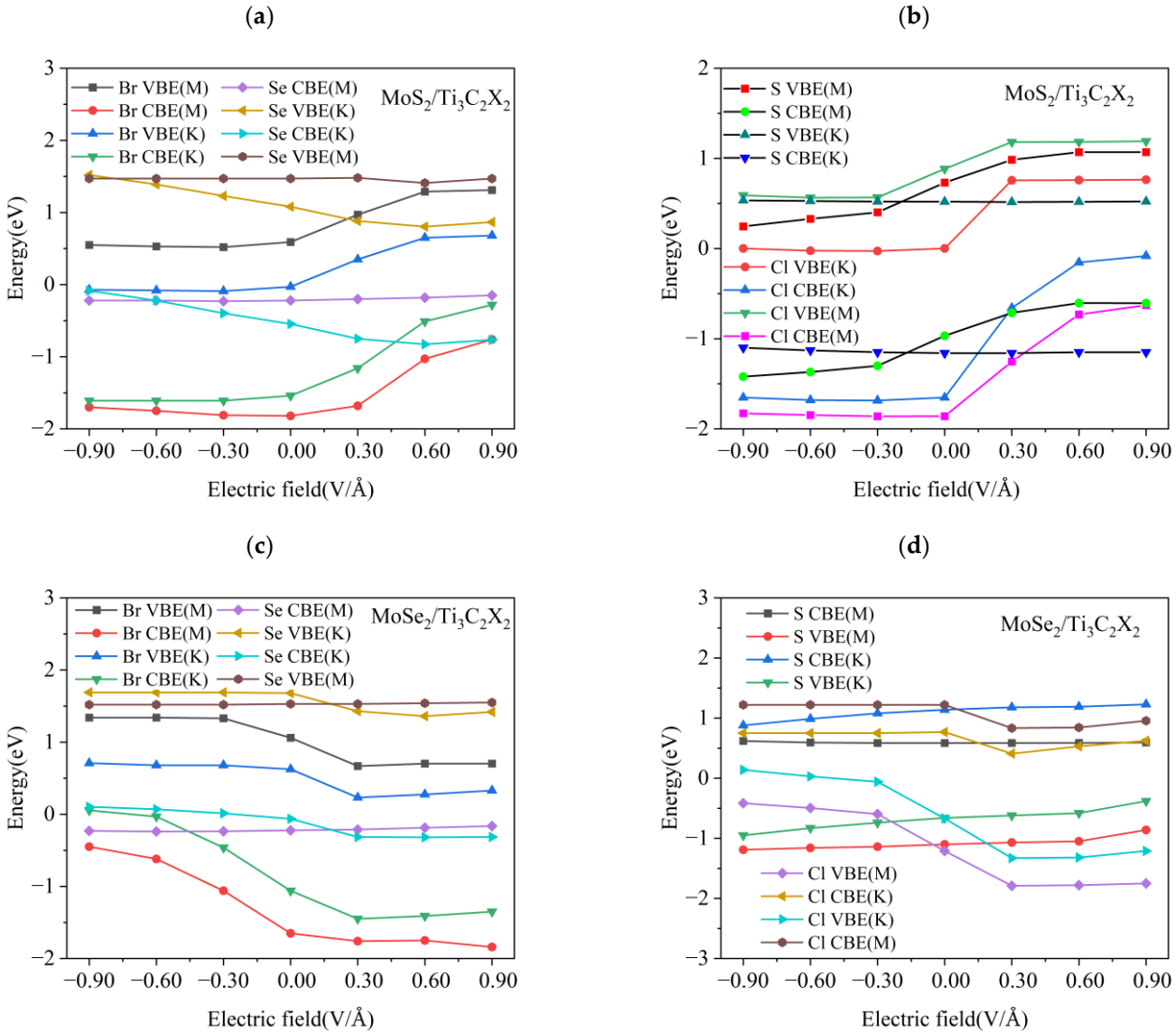


**Figure 18.** (**a**) The VBE and CBE at M and K points of $MoS_2/Ti_3C_2Br_2$ and $MoS_2/Ti_3C_2Se_2$ under different electric fields. (**b**) The VBE and CBE at M and K points of $MoS_2/Ti_3C_2S_2$ and $MoS_2/Ti_3C_2Cl_2$ under different electric fields. (**c**) The VBE and CBE at M and K points of $MoSe_2/Ti_3C_2Se_2$ and $MoSe_2/Ti_3C_2Br_2$ under different electric fields. (**d**) The VBE and CBE at M and K points of $MoSe_2/Ti_3C_2S_2$ and $MoSe_2/Ti_3C_2Cl_2$ under different electric fields.

## 4. Conclusions

The effects of biaxial strain and functional groups as well as electric fields on the structural and electronic properties of TMDs/$Ti_3C_2$ heterostructures were systematically investigated based on the density functional theory method. The six possible configurations of $MoS_2/Ti_3C_2$ and $MoSe_2/Ti_3C_2$ heterostructure stacks were first designed, and then geometrically optimized. ZM_SA were identified as the most energetically stable structural types of $MoS_2/Ti_3C_2$ heterostructures with a binding energy of $-1.79$ meV/Å$^2$. The most energetically stable structure type of $MoSe_2/Ti_3C_2$ heterostructures was SA_ZM, its binding energy of $-1.03$ meV/Å$^2$. The surface functional groups (S, Se, Cl, Br) of the monolayer $Ti_3C_2$ resulted in the lattice expansion of TMDs/$Ti_3C_2X_2$ heterostructures, and

the $MoSe_2/Ti_3C_2Br_2$ heterostructure possessed the maximum lattice parameters (3.262 Å). The conductivity of $MoS_2/Ti_3C_2$ and $MoSe_2/Ti_3C_2$ can be enhanced by increasing the biaxial tensile strain. When the surface of the monolayer $Ti_3C_2$ was occupied by S, Se, Cl, or Br, the coupling strength between the monolayer TMDs and $Ti_3C_2$ was obviously weakened, while the biaxial strain effectively improved their interaction strength. The different surface functional groups induced a different response of the electronic properties of TMDs/$Ti_3C_2X_2$ heterostructures to the external electric field. The energy bands around the Fermi energy level of TMDs/$Ti_3C_2X_2$ heterostructures obviously changed under the combined effect of surface functional groups with an electric field. These results demonstrated that TMDs/$Ti_3C_2X_2$ (X = S, Se, Cl, Br) heterostructures possess rich electronic properties. Moreover, both $MoS_2/Ti_3C_2X_2$ (X = Se, Br) and $MoSe_2/Ti_3C_2X_2$ (X = S, Se, Cl, Br) are rather sensitive to an external strain field, while only TMDs/$Ti_3C_2X_2$ (X = Cl, Br) strongly depends on an external positive electric field. We hope that these studies can provide a theoretical foundation for the application of TMDs/MXenes heterostructures in the field of high-performance nanoelectronic devices.

**Supplementary Materials:** The following supporting information can be downloaded at: https://www.mdpi.com/article/10.3390/nano13071218/s1, Figure S1: A schematic diagram of top and side views of $MoSe_2/Ti_3C_2$ heterostructures for different stackings; Figure S2: Band structures and densities of states of the $MoS_2$; Figure S3: Band structures and densities of states of the $MoSe_2$; Figure S4: The DOS of $MoSe_2/Ti_3C_2X_2$ and PDOS of $MoSe_2$ in $MoSe_2/Ti_3C_2X_2$ heterostructures under different electric fields. (a) X-Br, (b) X-Cl, (c) X-Se and (d) X-S; Figure S5: Density of states of the $MoS_2/Ti_3C_2Cl_2$ heterostructure with different biaxial strains; Figure S6: Density of states of the $MoS_2/Ti_3C_2S_2$ heterostructure with different biaxial strains; Figure S7: Density of states of the $MoSe_2/Ti_3C_2Cl_2$ heterostructure with different biaxial strains; Figure S8: Density of states of the $MoSe_2/Ti_3C_2S_2$ heterostructure with different biaxial strains; Table S1: Optimized structural parameters for the TMDs/$Ti_3C_2X_2$ (X = S, Se, Br, Cl) heterostructure; Table S2: Mulliken charge (electron), bond length (Å) and bond populations of $MoS_2/Ti_3C_2$; Table S3: Mulliken charge (electron), bond length (Å) and bond populations of $MoSe_2/Ti_3C_2$.

**Author Contributions:** S.Z.: Data curation, Formal analysis, Investigation, Methodology, Resources, Software, Validation, Visualization, Roles/Writing—original draft, Writing-review & editing. C.L.: Conceptualization, Investigation, Methodology, Funding acquisition, Project administration, Supervision, Validation, Writing—review & editing. C.W.: Investigation, Visualization. D.M.: Investigation, Visualization. B.W.: Investigation, Visualization. All authors have read and agreed to the published version of the manuscript.

**Funding:** This research was funded by the National Natural Science Foundation of China (12172097) and the Natural Science Foundation of Heilongjiang Province, China (LH2021A006). And The APC was funded by the National Natural Science Foundation of China (12172097).

**Data Availability Statement:** Data are available on request from the corresponding author.

**Conflicts of Interest:** The authors declare that there is no conflict of interest regarding publication of this manuscript.

## References

1. Chen, H.L.; Han, J.N.; Deng, X.Q.; Fan, Z.Q.; Sun, L.; Zhang, Z.H. Vertical Strain and Twist Induced Tunability on Electronic and Optical Properties of Janus HfSSe/SnC Van der Waals Heterostructure. *Appl. Surf. Sci.* **2022**, *598*, 153756. [CrossRef]
2. Wang, J.L.; Zhao, X.W.; Hu, G.C.; Ren, J.F.; Yuan, X.B. Manipulable Electronic and Optical Properties of Two-Dimensional MoSTe/$MoGe_2N_4$ van der Waals Heterostructures. *Nanomaterials* **2022**, *11*, 3338. [CrossRef] [PubMed]
3. Zhang, W.S.; Chen, J.; Wang, X.D.; Huang, H.; Yao, M. First-Principles Study of Transition Metal Ti-Based MXenes ($Ti_2MC_2T_x$ and $M_2TiC_2T_x$) as Anode Materials for Sodium-Ion Batteries. *ACS Appl. Nano Mater.* **2022**, *5*, 2358–2366. [CrossRef]
4. Huang, H.X.; Zha, J.J.; Li, S.S.; Tan, C.L. Two-dimensional alloyed transition metal dichalcogenide nanosheets: Synthesis and applications. *Chin. Chem. Lett.* **2022**, *33*, 163–176. [CrossRef]
5. Wang, Z.; Wang, P.; Wang, F.; Ye, J.F.; He, T.; Wu, F.; Peng, M.; Wu, P.; Chen, Y.; Zhong, F.; et al. A Noble Metal Dichalcogenide for High-Performance Field-Effect Transistors and Broadband Photodetectors. *Adv. Funct. Mater.* **2020**, *30*, 1907945. [CrossRef]
6. Na, J.; Park, C.; Lee, C.H.; Choi, W.R.; Choi, S.; Lee, J.U.; Yang, W.; Cheong, H.; Campbell, E.E.B.; Jhang, S.H. Indirect Band Gap in Scrolled $MoS_2$ Monolayers. *Nanomaterials* **2022**, *12*, 3353. [CrossRef]

7. Cai, Z.Y.; Liu, B.L.; Zou, X.L.; Cheng, H.-M. Chemical vapor deposition growth and applications of two-dimensional materials and their heterostructures. *Chem. Rev.* **2018**, *118*, 6091–6133. [CrossRef]
8. Tan, T.; Jiang, X.T.; Wang, C.; Yao, B.C.; Zhang, H. 2D material optoelectronics for information functional device applications: Status and challenges. *Adv. Sci.* **2020**, *7*, 2000058. [CrossRef]
9. Kuzel, P.; Nemec, H. Terahertz spectroscopy of nanomaterials: A close look at charge-carrier transport. *Adv. Opti. Mater.* **2020**, *8*, 1900623. [CrossRef]
10. Bafekry, A.; Stampfl, C.; Ghergherehchi, M. Strain, electric-field and functionalization induced widely tunable electronic properties in $MoS_2/BC_3$, $/C_3N$ and $/C_3N_4$ van der Waals heterostructures. *Nanotechnology* **2020**, *31*, 295202. [CrossRef]
11. Biroju, R.K.; Das, D.; Sharma, R.; Pal, S.; Mawlong, L.P.L.; Bhorkar, K.; Giri, P.K.; Singh, A.K.; Narayanan, T.N. Hydrogen evolution reaction activity of graphene-$MoS_2$ van der Waals heterostructures. *ACS Energy. Lett.* **2017**, *2*, 1355–1361. [CrossRef]
12. Li, J.T.; Zhou, X.L. First principles calculations of electrical and optical properties of $Cu_3N/MoS_2$ heterostructure with tunable bandgaps. *Appl. Phys. A* **2021**, *127*, 693. [CrossRef]
13. Yelgel, C. First-principles modeling of $GaN/MoSe_2$ van der Waals heterobilayer. *Turk. J. Phys.* **2017**, *41*, 463–468. [CrossRef]
14. Pogorielov, M.; Smyrnova, K.; Kyrylenko, S.; Gogotsi, O.; Zahorodna, V.; Pogrebnjak, A. MXenes-A New Class of Two-Dimensional Materials: Structure, Properties and Potential Applications. *Nanomaterials* **2022**, *11*, 3412. [CrossRef]
15. Fleischmann, S.; Mitchell, J.B.; Wang, R.; Zhan, C.; Jiang, D.-E.; Presser, V.; Augustyn, V. Pseudocapacitance: From fundamental understanding to high power energy storage materials. *Chem. Rev.* **2020**, *120*, 6738–6782. [CrossRef]
16. Hasan, M.M.; Hossain, M.M.; Chowdhury, H.K. Two-dimensional MXene-based flexible nanostructures for functional nanodevices: A review. *J. Mater. Chem A* **2021**, *9*, 3231–3269. [CrossRef]
17. Jiang, Q.; Lei, Y.J.; Liang, H.F.; Xi, K.; Xia, C.; Alshareef, H.N. Alshareef, Review of MXene electrochemical microsupercapacitors. *Energy Storage Mater.* **2020**, *27*, 78–95. [CrossRef]
18. Xiong, D.B.; Li, X.F.; Bai, Z.M.; Lu, S.G. Recent advances in layered $Ti_3C_2T_x$ MXene for electrochemical energy storage. *Small* **2018**, *14*, 1703419. [CrossRef]
19. Li, L.; Cao, H.H.; Liang, Z.S.; Cheng, Y.F.; Yin, T.T.; Liu, Z.Y.; Yan, S.W.; Jia, S.F.; Li, L.Y.; Wang, J.B.; et al. First-principles study of Ti-deficient $Ti_3C_2$ MXene nanosheets as $NH_3$ gas sensors. *ACS Appl. Nano Mater.* **2022**, *5*, 2470–2475. [CrossRef]
20. Li, D.Q.; Chen, X.F.; Xiang, P.; Du, H.Y.; Xiao, B.B. Chalcogenated-$Ti_3C_2X_2$ MXene (X = O, S, Se and Te) as a high-performance anode material for Li-ion batteries. *Appl. Surf. Sci.* **2020**, *501*, 144221. [CrossRef]
21. Mathis, T.S.; Maleski, K.; Goad, A.; Sarycheva, A.; Anayee, M.; Foucher, A.C.; Hantanasirisakul, K.; Shuck, C.E.; Stach, E.A.; Gogotsi, Y. Modified MAX phase synthesis for environmentally stable and highly conductive $Ti_3C_2$ MXene. *ACS Nano* **2021**, *15*, 6420–6429. [CrossRef] [PubMed]
22. Li, C.L.; Guo, J.; Wang, C.Y.; Ma, D.C.; Wang, B.L. Design of MXene contacts for high-performance WS2 transistors. *Appl. Surf. Sci.* **2020**, *527*, 146701. [CrossRef]
23. Liang, P.H.; Xu, T.F.; Zhu, K.J.; Rao, Y.; Zheng, H.J.; Wu, M.; Chen, J.T.; Liu, J.S.; Yan, K.; Wang, J. Heterogeneous interface-boosted zinc storage of $H_2V_3O_8$ nanowire/$Ti_3C_2T_x$ MXene composite toward high-rate and long cycle lifespan aqueous zinc-ion batteries. *Energy Storage Mater.* **2022**, *50*, 63–74. [CrossRef]
24. Ariga, K. Don't forget Langmuir-Blodgett films 2020: Interfacial nanoarchitectonics with molecules, materials, and living objects. *Langmuir* **2020**, *36*, 7158–7180. [CrossRef] [PubMed]
25. Nahirniak, S.; Ray, A.; Saruhan, B. Challenges and Future Prospects of the MXene-Based Materials for Energy Storage Applications. *Batteries* **2023**, *9*, 126. [CrossRef]
26. Yu, L.; Hu, L.F.; Anasori, B.; Liu, Y.-T.; Zhu, Q.Z.; Zhang, P.; Gogotsi, Y.; Xu, B. MXene-Bonded activated carbon as a flexible electrode for high-performance supercapacitors. *ACS Energy Lett.* **2018**, *3*, 1597–1603. [CrossRef]
27. Shen, C.J.; Wang, L.B.; Zhou, A.G.; Wang, B.; Wang, X.L.; Lian, W.W.; Hu, Q.K.; Qin, G.; Liu, X.Q. Synthesis and Electrochemical Properties of Two-Dimensional RGO/$Ti_3C_2T_x$ Nanocomposites. *Nanomaterials* **2018**, *8*, 80. [CrossRef]
28. Wu, W.L.; Zhao, C.H.; Niu, D.J.; Zhu, J.F.; Wei, D.; Wang, C.W.; Wang, L.; Yang, L.Q. Ultrathin N-doped $Ti_3C_2$-MXene decorated with $NiCo_2S_4$ nanosheets as advanced electrodes for supercapacitors. *Appl. Surf. Sci.* **2021**, *539*, 148272. [CrossRef]
29. Debow, S.; Zhang, T.; Liu, X.S.; Song, F.Z.; Qian, Y.Q.; Han, J.; Maleski, K.; Zander, Z.B.; Creasy, W.R.; Kuhn, D.L. Charge dynamics in $TiO_2$/MXene composites. *J. Phys. Chem. C* **2021**, *125*, 10473–10482. [CrossRef]
30. Jing, H.R.; Ling, F.L.; Liu, X.Q.; Chen, Y.K.; Zeng, W.; Zhang, Y.X.; Fang, L.; Zhou, M. Strain-engineered robust and Schottky-barrier-free contact in 2D metal-semiconductor heterostructure. *Electron. Struct.* **2019**, *1*, 015010. [CrossRef]
31. Guan, Q.Y.; Yan, H.J.; Cai, Y.Q. Flatten the Li-ion Activation in Perfectly Lattice-Matched MXene and 1T-$MoS_2$ Heterostructures via Chemical Functionalization. *Adv. Mater. Interfaces* **2022**, *9*, 2101838. [CrossRef]
32. Li, C.L.; Wu, G.X.; Wang, C.Y.; Fu, Y.; Wang, B.L. Tuning electronic and transport properties of $MoS_2/Ti_2C$ heterostructure by external strain and electric field. *Comput. Mater. Sci.* **2018**, *153*, 417–423. [CrossRef]
33. Xu, E.Z.; Zhang, Y.; Wang, H.; Zhu, Z.F.; Quan, J.J.; Chang, Y.J.; Li, P.C.; Yu, D.B.; Jiang, Y. Ultrafast kinetics net electrode assembled via $MoSe_2$/MXene heterostructure for high-performance sodium-ion batteries. *Chem. Eng. J.* **2020**, *385*, 123839. [CrossRef]
34. Ling, F.L.; Kang, W.; Jing, H.R.; Zeng, W.; Chen, Y.K.; Liu, X.Q.; Zhang, Y.X.; Zhou, M. Enhancing hydrogen evolution on the basal plane of transition metal dichacolgenide van der Waals heterostructures. *NPJ Comput. Mater.* **2019**, *5*, 20. [CrossRef]
35. Kamysbayev, V.; Filatov, A.S.; Hu, H.C.; Rui, X.; Lagunas, F.; Wang, D.; Klie, R.F.; Talapin, D.V. Covalent surface modifications and superconductivity of two-dimensional metal carbide MXenes. *Science* **2020**, *369*, 979–983. [CrossRef]

36. Clark, S.J.; Segall, M.D.; Pickard, C.J.; Hasnip, P.J.; Probert, M.I.J.; Refson, K.; Payne, M.C. First principles methods using CASTEP, Z. Krist-Cryst. *Materials* **2005**, *220*, 567–570.
37. Perdew, J.P.; Burke, K.; Ernzerhof, M. Generalized gradient approximation made simple. *Phys. Rev. Lett.* **1996**, *77*, 3865–3868. [CrossRef]
38. McNellis, E.R.; Meyer, J.; Reuter, K. Azobenzene at coinage metal surfaces: Role of dispersive van der Waals interactions. *Phys. Rev. B* **2009**, *80*, 205414. [CrossRef]
39. Ding, Y.C.; Xiao, B.; Li, J.L.; Deng, Q.; Xu, Y.H.; Wang, H.F.; Rao, D.W. Improved transport properties and novel Li diffusion dynamics in van der waals $C_2N$/graphene heterostructure as anode materials for lithium-ion batteries: A first-principles investigation. *J. Phys. Chem. C* **2019**, *123*, 3353–3367. [CrossRef]
40. Ibragimova, R.; Lv, Z.P.; Komsa, H.P. First principles study of the stability of MXenes under an electron beam. *Nanoscale Adv.* **2021**, *3*, 1934–1941. [CrossRef]
41. Yu, Y.X. Can all nitrogen-doped defects improve the performance of graphene anode materials for lithium-ion batteries? *Phys. Chem. Chem. Phys.* **2013**, *15*, 16819–16827. [CrossRef] [PubMed]
42. Froyen, S. Brillouin-zone integration by Fourier quadrature: Special points for superlattice and supercell calculations. *Phys. Rev. B* **1989**, *39*, 3168–3172. [CrossRef]
43. Zeng, L.H.; Wu, D.; Jie, J.S.; Ren, X.Y.; Hu, X.; Lau, S.P.; Chai, Y.; Tsang, Y.H. Van der Waals epitaxial growth of mosaic-like 2D platinum ditelluride layers for room-temperature mid-infrared photodetection up to 10.6 μm. *Adv. Mater.* **2020**, *32*, 2004412. [CrossRef] [PubMed]
44. Choi, D.; Kang, J.; Park, J.; Han, B. First-principles study on thermodynamic stability of the hybrid interfacial structure of $LiMn_2O_4$ cathode and carbonate electrolyte in Li-ion batteries. *Phys. Chem. Chem. Phys.* **2018**, *20*, 11592–11597. [CrossRef] [PubMed]
45. Bandeira, N.S.; da Costa, D.R.; Chaves, A.; Farias, G.A.; Filho, R.N.C. Gap opening in graphene nanoribbons by application of simple shear strain and in-plane electric field. *J. Phys. Condens. Matter* **2020**, *33*, 065503. [CrossRef]
46. Hu, T.; Wang, J.M.; Zhang, H.; Li, Z.J.; Hu, M.M.; Wang, X.H. Vibrational properties of $Ti_3C_2$ and $Ti_3C_2T_2$(T = O, F, OH) monosheets by first-principles calculations: A comparative study. *Phys. Chem. Chem. Phys.* **2015**, *17*, 9997–10003. [CrossRef]
47. Lindroth, D.O.; Erhart, P. Thermal transport in van der Waals solids from first-principles calculations. *Phys. Rev. B* **2016**, *94*, 115205. [CrossRef]
48. Frechette, L.B.; Dellago, C.; Geissler, P.L. Consequences of lattice mismatch for phase equilibrium in heterostructured solids. *Phys. Rev. Lett.* **2019**, *123*, 135701. [CrossRef]
49. Zhang, Z.H.; Zhang, Y.; Xie, Z.F.; Wei, X.; Guo, T.T.; Fan, J.B.; Ni, L.; Tian, Y.; Liu, J.; Duan, L. Tunable electronic properties of an Sb/InSe van der Waals heterostructure by electric field effects. *Phys. Chem. Chem. Phys.* **2019**, *10*, 5627–5633. [CrossRef]
50. Hanbicki, A.T.; Chuang, H.J.; Rosenberger, M.R.; Hellberg, C.S.; Sivaram, S.V.; McCreary, K.M.; Mazin, I.I.; Jonker, B.T. Double indirect interlayer exciton in a $MoSe_2/WSe_2$ van der Waals heterostructure. *ACS Nano* **2018**, *5*, 4719–4726. [CrossRef]
51. Li, N.; Fan, J. Computational insights into modulating the performance of MXene based electrode materials for rechargeable batteries. *Nanotechnology* **2021**, *32*, 252001. [CrossRef] [PubMed]
52. Robert, C.; Han, B.; Kapuscinski, P.; Delhomme, A.; Faugeras, C.; Amand, T.; Molas, M.R.; Marie, X. Measurement of the spin-forbidden dark excitons in $MoS_2$ and $MoSe_2$ monolayers. *Nat. Commun.* **2020**, *11*, 4037. [CrossRef] [PubMed]
53. Ahn, G.H.; Amani, M.; Rasool, H.; Lien, D.-H.; Mastandrea, J.P.; Iii, J.W.A.; Dubey, M.; Chrzan, D.C.; Minor, A.M.; Javey, A. Strain-engineered growth of two-dimensional materials. *Nat. Commun.* **2017**, *8*, 608. [CrossRef] [PubMed]
54. Yang, S.X.; Chen, Y.J.; Jiang, C.B. Strain engineering of two-dimensional materials: Methods, properties, and applications. *InfoMat* **2021**, *3*, 397–420. [CrossRef]
55. Saha, S.; Samanta, P.; Murmu, N.C.; Kuila, T. A review on the heterostructure nanomaterials for supercapacitor application. *J. Energy Storage* **2018**, *17*, 181–202. [CrossRef]
56. Ouyang, W.X.; Teng, F.; Fang, X.S. High performance BiOCl nanosheets/$TiO_2$ nanotube arrays heterojunction UV photodetector: The influences of self-induced inner electric fields in the BiOCl nanosheets. *Adv. Funct. Mater.* **2018**, *28*, 1707178. [CrossRef]
57. Chen, X.J.; Wang, J.; Chai, Y.Q.; Zhang, Z.J.; Zhu, Y.F. Efficient photocatalytic overall water splitting induced by the giant internal electric field of a g-$C_3N_4$/rGO/PDIP Z-scheme heterojunction. *Adv. Mater.* **2021**, *33*, 2007479. [CrossRef]